6-2014

On the Dynamics, Thermodynamics, and Forecast Model Evaluation of Two Snow-Burst Events in Southern Alberta

Shawn M. Milrad
Embry-Riddle Aeronautical University, milrads@erau.edu

John R. Gyakum
McGill University

Kelly Lombardo
University of Connecticut - Avery Point

Eyad H. Atallah
McGill University

On the Dynamics, Thermodynamics, and Forecast Model Evaluation of Two Snow-Burst Events in Southern Alberta

SHAWN M. MILRAD

Applied Aviation Sciences Department, Embry-Riddle Aeronautical University, Daytona Beach, Florida

JOHN R. GYAKUM

Department of Atmospheric and Oceanic Sciences, McGill University, Montreal, Quebec, Canada

KELLY LOMBARDO

Department of Marine Sciences, University of Connecticut—Avery Point, Groton, Connecticut

EYAD H. ATALLAH

Department of Atmospheric and Oceanic Sciences, McGill University, Montreal, Quebec, Canada

(Manuscript received 18 August 2013, in final form 14 March 2014)

ABSTRACT

Two high-impact convective snowband events ("snow bursts") that affected Calgary, Alberta, Canada, are examined to better understand the dynamics and thermodynamics of heavy snowbands not associated with lake effects or the cold conveyor belt of synoptic-scale cyclones. Such events are typically characterized by brief, but heavy, periods of snow; low visibilities; and substantial hazards to automobile and aviation interests. Previous literature on these events has been limited to a few case studies across North America, including near the leeside foothills of the U.S. Rockies. The large-scale dynamics and thermodynamics are investigated using the National Centers for Environmental Prediction (NCEP) North American Regional Reanalysis (NARR). Previously, high-resolution convection-explicit Weather Research and Forecasting Model (WRF) simulations have shown some ability to successfully reproduce the dynamics, thermodynamics, and appearance of convective snowbands, with small errors in location and timing. Therefore, WRF simulations are performed for both events, and are evaluated along with the NCEP North American Mesoscale (NAM) model forecasts. Both the NARR and WRF simulations show that while the two snow bursts are similar in appearance, they form as a result of different dynamic and thermodynamic mechanisms. The first event occurs downstream of an upper-tropospheric jet streak in a region of little synoptic-scale ascent, where ageostrophic frontogenesis helps to release conditional, dry symmetric, and inertial instability in an unsaturated environment. The inertial instability is determined to be related to fast flow over upstream high terrain. The second event occurs in a saturated environment in a region of **Q**-vector convergence (primarily geostrophic frontogenesis), which acts to release conditional, convective, and conditional symmetric instability (CSI).

1. Introduction

DeVoir (2004), Pettegrew et al. (2009), Schumacher et al. (2010), and Milrad et al. (2011, hereinafter MGAS11) were the first publications to document the dynamics and thermodynamics of non-lake-effect snow squalls ("snow bursts"). Such events are generally characterized by convective bands of moderate to heavy snow, a cold frontal passage, relatively small snow accumulations, short-lived very low visibilities, and large impacts on both automobile and aviation interests (e.g., MGAS11; Makela et al. 2013; Pettegrew et al. 2009). MGAS11 distinguished these events from lake-effect snowsqualls and heavy banded precipitation within the cold conveyor belt of synoptic-scale cyclones (e.g., Nicosia and Grumm 1999; Novak et al. 2004; 2006; 2009; 2010). A literature review on convective snowbands is available in MGAS11 and references therein.

Corresponding author address: Shawn M. Milrad, Applied Aviation Sciences Dept., Embry-Riddle Aeronautical University, 600 S. Clyde Morris Blvd., Daytona Beach, FL 32119.
E-mail: shawn.milrad@gmail.com

DOI: 10.1175/WAF-D-13-00099.1

TABLE 1. Raw METAR reports at CYYC from 2100 UTC 3 Dec ($t = -3$ h) through 0600 UTC 4 Dec 2011 ($t = +6$ h), during the passage of CSB1. The observations from $t = 0$ h are set in boldface italics.

2100 UTC 3 Dec–0600 UTC 4 Dec 2011
CYYC 032100Z 31014KT 4SM -SN OVC011 00/M02 A2998 RMK SC8 VIS HIER SW SLP208
CYYC 032200Z 29007KT 40SM -SN BKN040 OVC090 00/M01 A2998 RMK SC6AC2 PCPN VRY LGT SLP210
CYYC 032300Z 31011KT 20SM FEW015 BKN030 OVC110 02/M03 A2998 RMK SC2SC3AC1 SLP209
CYYC 040000Z 36020G28KT 1/2SM SN VV002 M02/M02 A3004 RMK SN8 RVR RWY34 4500 FT SLP233
CYYC 040100Z 35020G26KT 5SM -SN SCT030 BKN040 OVC070 M02/M04 A3007 RMK SC3SC3AC2 SLP241
CYYC 040200Z 35013KT 5SM -SN SCT015 OVC040 M03/M04 A3009 RMK SC3SC5 SLP249
CYYC 040300Z 34009KT 2 1/2SM -SN BR SCT007 OVC026 M03/M03 A3011 RMK SC3SC5 SLP249
CYYC 040400Z 36015KT 1 1/2SM -SN BR SCT011 OVC023 M04/M05 A3015 RMK SC4SC4 SLP262
CYYC 040500Z 36014KT 2 1/2SM -SN DRSN SCT008 OVC023 M05/M06 A3017 RMK SC3SC5 SLP269
CYYC 040600Z 36014KT 1 1/2SM -SN DRSN SCT010 OVC025 M05/M06 A3022 RMK SC3SC5 SLP286

MGAS11 discussed two snow bursts in eastern Ontario, Canada, that occurred on the same day in January 2010, while Pettegrew et al. (2009) focused on a similar event that took place in Illinois and Indiana. Here, we turn our attention to two snow bursts that impacted the Calgary, Alberta, Canada, region in December 2011 and January 2013, respectively. These two events are examples of snow bursts in a region (the foothills of the Rockies) in which mesoscale convective snowbands have been previously examined by, for example, Schultz and Knox (2007), Andretta and Geerts (2010), and Schumacher et al. (2010).

The first event (hereinafter Calgary snow burst 1, CSB1) occurred on the evening of 3 December 2011 (Table 1). Wood (2011) reported that the city of Calgary's emergency services responded to 12 automobile collisions at approximately the same time during the height of the event, as "hard and fast bursts of snow" fell. The Calgary Police Service also stated that "we had an awful lot of snow in a very short period of time and it was. . .unexpected." (Wood 2011). MGAS11 and DeVoir (2004) documented similar tales, as these events often escalate quickly and occur without much forecast or warning lead time (Schumacher et al. 2010). Our second event (hereinafter Calgary snow burst 2, CSB2) occurred during the evening and overnight of 9–10 January 2013, peaking at 0300 UTC 10 January (Table 2). Ho (2013) stated that there were 45 automobile crashes reported in the Calgary metropolitan area during CSB2.

This study investigates the dynamics and thermodynamics of CSB1 and CSB2, within the context of the Pettegrew et al. (2009), Schumacher et al. (2010), and MGAS11 results, using 1) reanalysis data, 2) an operational numerical forecast model, and 3) high-resolution convection-explicit numerical model simulations.

The remainder of this paper is organized as follows. Section 2 details the data used, section 3 discusses the surface and radar observations of both cases, section 4 contains the synoptic–dynamic analysis using reanalysis data, and section 5 discusses the numerical simulations. Section 6 provides a summary and avenues for future work.

2. Data

Radar data were obtained using the Environment Canada (EC) historical radar database (available online at http://www.climate.weatheroffice.gc.ca/radar/index_e.html). The data are from the radar closest to Calgary

TABLE 2. Raw METAR reports at CYYC from 0000 UTC ($t = -3$ h) through 0900 UTC ($t = +6$ h) 10 Jan 2013, during the passage of CSB2. The observations from $t = 0$ h are set in boldface italics. Special reports issued between hourly observations are included.

0000–0900 UTC 10 Jan 2013
CYYC 100000Z 03013KT 220V040 25SM FEW040 SCT140 SCT200 M01/M06 A2944 RMK SC1AC2CC1 BIRDS MOVG N-S PRESRR SLP025
CYYC 100100Z 34018G24KT 15SM FEW030 BKN100 OVC200 M06/M09 A2947 RMK SC2AC4CC2 SLP040
CYYC 100200Z 34018G24KT 2SM -SN BKN020 OVC030 M05/M07 A2949 RMK SN2ST4SC2 SLP047
CYYC 100208Z 34018G25KT 1/2SM -SN BKN003 OVC012 M05/M07 A2950 RMK SN4ST2SC2 SLP049
CYYC 100300Z 34017G24KT 5/8SM R28/3000V5000FT/N SN BKN003 OVC015 M05/M06 A2953 RMK SN3ST3SC2 PRESRR SLP050
CYYC 100400Z 34016KT 5/8SM R28/5000VP6000FT/U SN BKN004 OVC013 M05/M06 A2959 RMK SN2ST4SC2 /S05/ SLP063
CYYC 100447Z 35015G24KT 1 1/2SM -SN OVC015 M05/M07 A2961 RMK SC8/S07/PRESRR SLP072
CYYC 100500Z 34017G22KT 2SM -SN BKN016 OVC030 M05/M07 A2962 RMK SC5SC3/S08/PRESRR SLP076
CYYC 100600Z 35019KT 4SM -SN BKN025 BKN040 OVC090 M06/M08 A2965 RMK SC5SC2AC1 SLP082
CYYC 100700Z 34018KT 6SM -SN FEW025 BKN050 OVC070 M06/M08 A2967 RMK SC2SC4AC2 PCPN VRY LGT SLP092
CYYC 100800Z 34017G25KT 15SM BKN018 OVC050 M06/M08 A2970 RMK SC5SC3 SLP100
CYYC 100900Z 34017G24KT 15SM BKN011 OVC020 M06/M08 A2975 RMK SC5SC3 SLP117

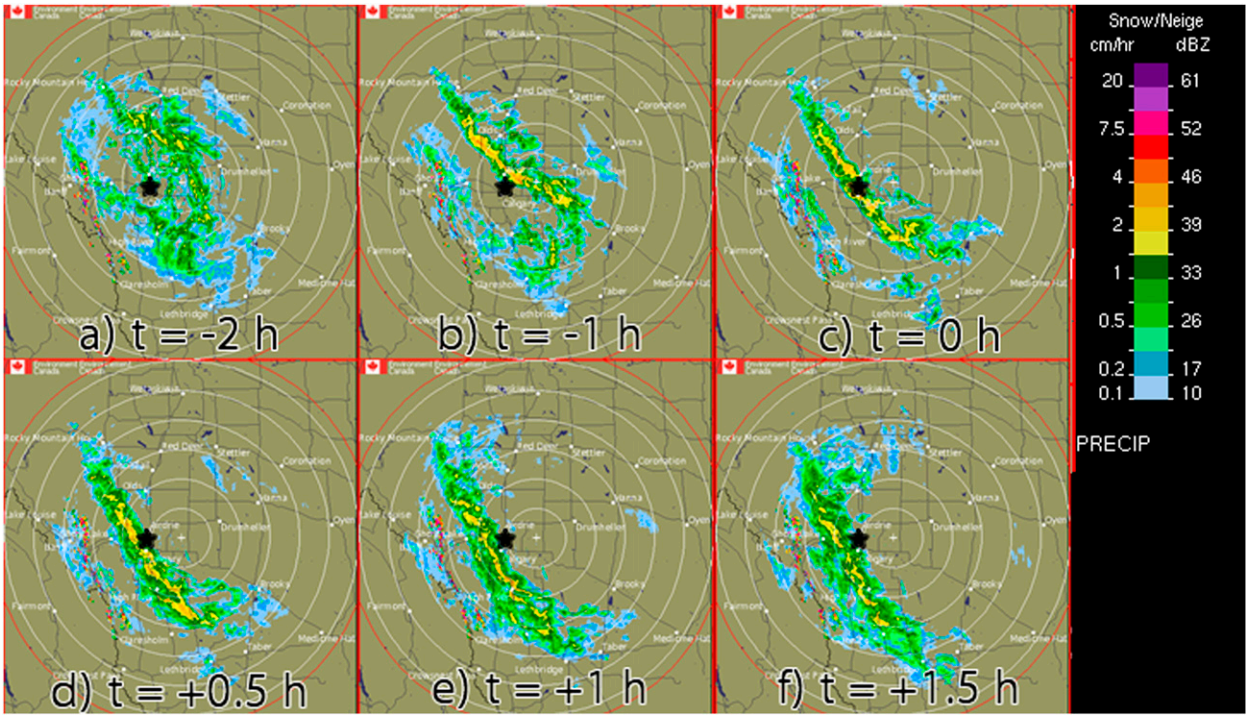

FIG. 1. For CSB1, EC radar imagery (CAPPI) from the Strathmore (Calgary) radar for 3–4 Dec 2011 at (a) 2200 UTC 3 Dec ($t = -2$ h), (b) 2300 UTC 3 Dec ($t = -1$ h), (c) 0000 UTC 4 Dec ($t = 0$ h), (d) 0030 UTC 4 Dec ($t = +0.5$ h), (e) 0100 UTC 4 Dec ($t = +1$ h), and (f) 0130 UTC 4 Dec ($t = +1.5$ h). The approximate location of the Calgary International Airport (CYYC) is marked with a black star.

(CYYC), located near Strathmore, Alberta (CXSM), approximately 50 km east-northeast of CYYC. As stated in MGAS11, EC radars are C-band radars with a wavelength of 5 cm and a beamwidth of 0.65°. These radars operate in a continuous scanning mode with a typical volume scan that lasts 5 min, and have a Doppler coverage area that is approximately 256 km in diameter. In the cool season, EC radars generally operate in snow precipitation mode (Environment Canada 2013a). Typical EC radar images (including in this paper) are constant altitude plan position indicator (CAPPI; Environment Canada 2013a).

Surface data were obtained from Iowa State University's Iowa Environmental Mesonet archive (available online at http://mesonet.agron.iastate.edu/archive/). Precipitation data were acquired from the EC historical climate database (online at http://www.climate.weatheroffice.gc.ca/climateData/canada_e.html). For the synoptic–dynamic analysis, we utilized the National Centers for Environmental Prediction (NCEP) North American Regional Reanalysis (NARR), which has a grid spacing of 32 km and 3-h temporal resolution (Mesinger et al. 2006).

To evaluate numerical model forecasts, we used the NCEP North American Mesoscale (NAM) model, which has a grid spacing of 12 km, is run every 6 h, has forecast output for every 3 h through 84 h, and uses the Nonhydrostatic Mesoscale Model version of the Weather Research and Forecasting Model (WRF-NMM; Janjić et al. 2010). We also produced simulations using version 3.5 of the WRF with the Advanced Research core (WRF-ARW; Skamarock et al. 2008), details of which can be found in section 5. The NAM data were downloaded from the National Climatic Data Center (NCDC) model archive (available online at http://nomads.ncdc.noaa.gov/data.php?name=access#hires_weather_datasets).

All calculations and analyses in this study are displayed using the General Meteorological Package (GEMPAK) version 6.2.0, updated from the original package devised by Koch et al. (1983).

3. Case overviews

For each case, we define $t = 0$ h as the hour closest to the passage of each snow burst through CYYC. For CSB1, $t = 0$ h is 0000 UTC 4 December 2011, and for CSB2, $t = 0$ h is 0300 UTC 10 January 2013. Figures 1 and 2 show the radar evolution of CSB1 and CSB2, respectively, and Fig. 3 and Tables 1 and 2 present surface observations from both cases.

a. CSB1

Table 1 and Fig. 3a show aviation routine weather reports (METAR) for CYYC before, during, and after the

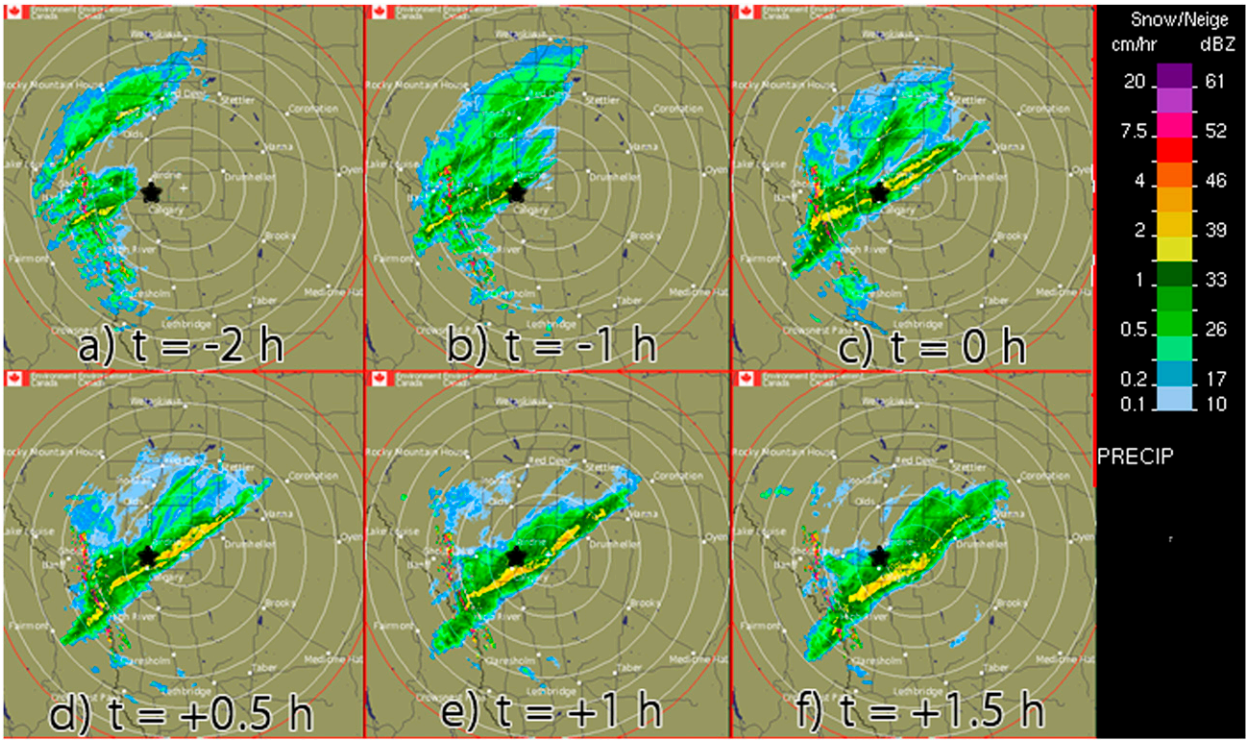

FIG. 2. For CSB2, EC radar imagery (CAPPI) from the Strathmore (Calgary) radar for 10 Jan 2013 at (a) 0100 UTC ($t = -2$ h), (b) 0200 UTC ($t = -1$ h), (c) 0300 UTC ($t = 0$ h), (d) 0330 UTC ($t = +0.5$ h), (e) 0400 UTC ($t = +1$ h), and (f) 0430 UTC ($t = +1.5$ h). The approximate location of CYYC is marked with a black star.

passage of CSB1. At $t = -1$ h (2300 UTC 3 December), the visibility at CYYC was 20 statute miles (sm; 1 sm = 1.609 km) and winds were relatively weak (11 kt, where 1 kt = 0.514 m s^{-1}) from the northwest. Dramatic changes occurred by $t = 0$ h: visibility fell to 0.5 sm, moderate snow was observed, northerly winds increased to 20 kt (gusting to 28 kt), mean sea level pressure (MSLP) increased 2.4 hPa, and 8 cm of snow fell in <1 h (Table 1). These observations depict the rapid deterioration of weather conditions often observed in snow-burst cases (DeVoir 2004; Pettegrew et al. 2009; MGAS11). As soon as CSB1 (Fig. 1) passed through CYYC, the visibility improved to 5 sm at $t = +1$ and +2 h (Table 1, Fig. 3a). CSB1 eventually slowed down and become nearly stationary, blocked by the higher terrain to the west of CYYC (Fig. 1).

Figure 1 shows that at $t = -2$h (Fig. 1a), a broad area of snow was located to the north and northeast of CYYC. By $t = -1$ h (Fig. 1b), a heavy (35+ dBZ) northwest–southeast-oriented band of snow (CSB1) was evident just northeast of CYYC; this rapid band organization was also observed in MGAS11. The orientation of the snow burst was similar to those of the convective snowbands in Schumacher et al. (2010), although the length and width of the strongest band (approximately 200 km; Fig. 1) were less than in the heaviest band in Schumacher et al. (2010). CSB1 (still 35+ dBZ) moved southwestward toward and through CYYC by $t = 0$ h (Fig. 1c), before stalling along the higher terrain west of Calgary at later times (Figs. 1e,f). Areas in the foothills of the Rockies received >20 cm of snow over the subsequent 12–24 h, aided by upslope northerly and northeasterly flow that started well after $t = 0$ h (not shown).

Table 1 and Fig. 3a also show that the snow-burst passage, temperature drop, and pressure rise all occurred around $t = 0$ h, supporting the assertion of a cold frontal passage. The temperature at CYYC was above freezing (+2°C) prior to the passage of CSB1 ($t = -1$ h), but dropped 7°C over the next 12 h (Table 1, Fig. 3a), as the wind remained brisk (10–20 kt) from the north. The visibilities in the hours after $t = 0$ h ranged from 1.5 to 5 sm in the presence of occasional light snow (Table 1, Fig. 3a), but moderate or heavy snow and associated low (≤0.5 sm) visibilities were not reported at CYYC after CSB1 moved through.

Finally, despite the METAR report of 8-cm accumulation in 1 h (Table 1), the EC official historical climate data reported only 6.6 cm of snow at CYYC for the entire day, which could be due to settling that occurred when the 6-h synoptic observation was taken. Either amount corresponds with previous studies (e.g., DeVoir 2004; Pettegrew et al. 2009; Schumacher et al. 2010;

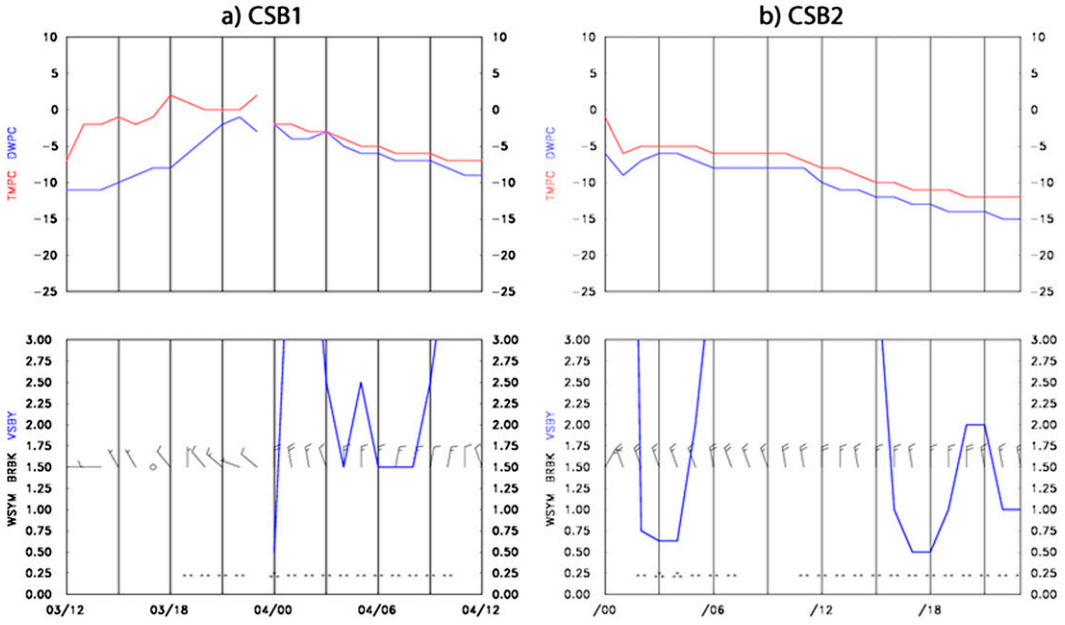

FIG. 3. Meteorograms for (a) CSB1 (1200 UTC 3 Dec–1200 UTC 4 Dec 2011) and (b) CSB2 (0000 UTC 9 Jan–0000 UTC 10 Jan 2013). In the (top) of (a) and (b), temperature (dewpoint) is plotted in red (blue) (°C). In the (bottom) of (a) and (b), visibility (sm) is on the vertical axis (blue; not shown for values >3 sm) and wind (kt) is represented by barbs. Data at $t = -1$ h for CSB1 were missing from the archive (see Table 1).

MGAS11) that found that snow accumulations during these types of events were generally light and below the snowfall warning criterion [15 cm in Canada; Environment Canada (2013b)].

b. CSB2

Figure 2 shows that unlike CSB1, CSB2 formed in situ over the Calgary region. The surface wind at CYYC began shifting direction 2–3 h prior to $t = 0$ h, from southwest to northeast, and finally to north-northwest (Table 2, Fig. 3b). The visibilities slowly deteriorated, decreasing from 15 sm at $t = -2$ h to approximately 0.5 sm just before and at $t = 0$ h (Table 2, Fig. 3b). As soon as the wind shifted to the north-northwest at $t = -2$ h, those winds persisted for the rest of the day (Fig. 3b), although the visibilities steadily improved after $t = +1$ h (Table 2, Fig. 3b). There were two reports of moderate snow at CYYC: at $t = 0$ and $+1$ h, as CSB2 moved through. There were no reports of heavy snow (Table 2, Fig. 3b).

Unlike CSB1, CSB2 was oriented northeast–southwest, a difference further discussed in sections 4 and 5. CSB2 originated as a broad, ill-defined area of snow west and northwest of CYYC at $t = -2$ h (Fig. 2a). By $t = -1$ h (Fig. 2b), the area of snow started to expand eastward toward CYYC, forming a well-defined heavy (35+ dBZ) band by $t = 0$ h (Fig. 2c). CSB2 moved southeast as the heaviest snow moved away from CYYC and toward southeastern Alberta (Fig. 2d-f).

Table 2 and Fig. 3b show that while the lowest visibility at CYYC was observed around $t = 0$ h, the wind shift and temperature drop did not occur with the snow burst's passage. The wind shift from southwest to north-northwest occurred around $t = -3$ and -2 h (Table 2), and a 5°C temperature drop also occurred during that time. This suggests that unlike CSB1, CSB2 moved through CYYC approximately 3 h postfrontal. MGAS11 also showed that snow bursts did not necessarily coincide with a frontal passage; the first case in MGAS11 occurred as the wind shifted, while the second case 2 h later was associated with falling temperatures and dewpoints.

Regarding snowfall accumulations, daily data for 9 January 2013 (when CSB2 moved through in mountain standard time) were missing in the EC historical database. However, the METAR reports suggest 8 cm fell between $t = 0$ and $+2$ h (including 5 cm from $t = 0$ to 1 h), and Ho (2013) cited EC having reported around 9 cm of total accumulation that day. Considering the relatively short duration of the snow (Table 2) and only two reports of moderate snow, it is unlikely that the total accumulation met the EC snowfall warning criterion (15 cm).

4. Synoptic–dynamic analysis

Doswell et al. (1996), Schultz and Schumacher (1999), and Wetzel and Martin (2001) proposed an ingredients-based methodology for moist convection, including

during the cold season. This was the approach taken by Schumacher et al. 2010 and MGAS11 and is generally followed here. The ingredients common to all studies were lift, moisture, and instability [both gravitational and symmetric (slantwise)]. Both Schumacher et al. (2010) and MGAS11 found that snow bursts occurred in generally subsaturated or near-saturated environments, particularly in the foothills of the Rockies. For the sake of brevity, an in-depth moisture analysis is not included in this paper, with the exception of comments on the level of atmospheric saturation in sections 4b and 5b. However, using NARR gridpoint data, we note that at $t = 0$ h at CYYC, the total-column precipitable water for CSB1 was 5.64 mm and was 6.53 mm for CSB2. These values are in accordance with the MGAS11 statements that described relatively small values of atmospheric moisture during snow bursts.

a. Lift

To diagnose lift, two forms of the adiabatic, frictionless QG omega equation are used: 1) the traditional form [Eq. (5.6.11) in Bluestein (1992)], which states that differential cyclonic vorticity advection (CVA) and a horizontal maximum in geostrophic warm-air advection (WAA) are indicative of ascent, and 2) the **Q**-vector form of the QG omega equation [Eq. (5.7.58) in Bluestein (1992)], in which **Q**-vector convergence is associated with ascent (Hoskins et al. 1978). For the first equation, we can assume that the sense of the midtropospheric vorticity advection is representative of differential vorticity advection. Henceforth, we use vorticity advection to refer to differential vorticity advection.

Miller (1948), Keyser et al. (1988), and Bluestein (1993) defined frontogenesis as the rate of change over time of the horizontal potential temperature gradient:

$$\mathbf{F}_p = \frac{D_p}{Dt}\nabla_p\theta, \tag{1}$$

where $\mathbf{F}_p$ is the vector frontogenetical function and θ is potential temperature. In accordance with Eq. (1), we use the 2D frontogenesis equation in our calculations, substituting the geostrophic, ageostrophic, or total wind as needed. Geostrophic frontogenesis can be related back to the **Q** vector and thus QG vertical motion using

$$\mathbf{Q} = \frac{R}{c_p}\left(\frac{p}{p_o}\right)^{\kappa}\mathbf{F}_p, \tag{2}$$

where **Q** is the **Q** vector, p is the pressure, p_o is some reference pressure, R is the gas constant for dry air, and κ is R divided by c_p, the specific heat at constant pressure. Frontogenesis and frontolysis are indicated when **Q** points to warmer and colder air, respectively (e.g., Sanders and Hoskins 1990).

Figure 4 shows that CSB1 occurs in the left-exit region of a straight northwest–southeast-upper-tropospheric jet streak (Fig. 4c), a region associated with ascent (e.g., Bluestein 1993). This is shown by upper-tropospheric CVA over CYYC at $t = 0$ h (Fig. 4c). Note that an upper-tropospheric trough is located to the east of the Calgary area from $t = -6$ h onward (Figs. 4a–c), suggesting that CVA related to shear vorticity in the jet streak is dominating CVA due to curvature (Fig. 4c). The northwest–southeast-oriented straight jet during CSB1 is remarkably similar to the large-scale pattern during the convective snowbands of Schumacher et al. (2010).

In CSB2, CYYC is in the entrance region of an anticyclonically curved jet streak (Figs. 4d–f), which Moore and Vanknowe (1992) defined as a region of upper-level divergence (i.e., CVA from shear vorticity). An upper-tropospheric trough is far upstream of CYYC, with a mesoridge located between the upstream trough and CYYC (Figs. 4d–f), and, accordingly, Fig. 4f shows CVA near CYYC at $t = 0$ h. We can conclude that in both CSB1 and CSB2, an upper-tropospheric jet streak is positioned such that CYYC is in a region favorable for ascent despite the differences between the upper-tropospheric height patterns (Fig. 3).

In MGAS11, 850–500-hPa **Q**-vector convergence (indicative of QG ascent) was observed prior to and at the time of the snow bursts, ahead of a midtropospheric trough. Here, we use the 850–250-hPa layer to account for QG ascent associated with jet streaks. In CSB1, a weak (1016 hPa) MSLP cyclone is observed northeast of Calgary at $t = -6$ and -3 h (Figs. 5a,b). Geostrophic cold-air advection (CAA, associated with QG descent) is observed at $t = -3$ and 0 h (Figs. 5b,c), as the MSLP cyclone moves away. The magnitude of contribution to vertical motion of upper-tropospheric CVA exceeds that of CAA at $t = -6$ and -3 h, as **Q**-vector convergence is observed (Figs. 5a,b). However, at $t = 0$ h, CYYC is in a region of neutral to slightly positive **Q**-vector divergence (QG descent; Fig. 5c), as CAA and CVA essentially cancel [Eq. (1)]. The position of CYYC to the southwest of the MSLP cyclone in a region of CAA (Fig. 5) is again quite similar to the Schumacher et al. (2010) case.

CSB2 features a stronger MSLP lee cyclone (998 hPa) than in CSB1 (Figs. 5d–f). The cyclone is centered downstream of the Calgary area, again placing CYYC in a region of geostrophic CAA, especially at $t = -3$ and 0 h (Figs. 5e,f). However, **Q**-vector convergence (QG ascent) is observed throughout (Figs. 5d–f), suggesting that CAA is negligible (or slight WAA exists) compared to CVA. The MSLP pattern is similar to the Davis (1997) type 2 case, in which a convective snowband also developed in a post-cold-frontal environment, associated with

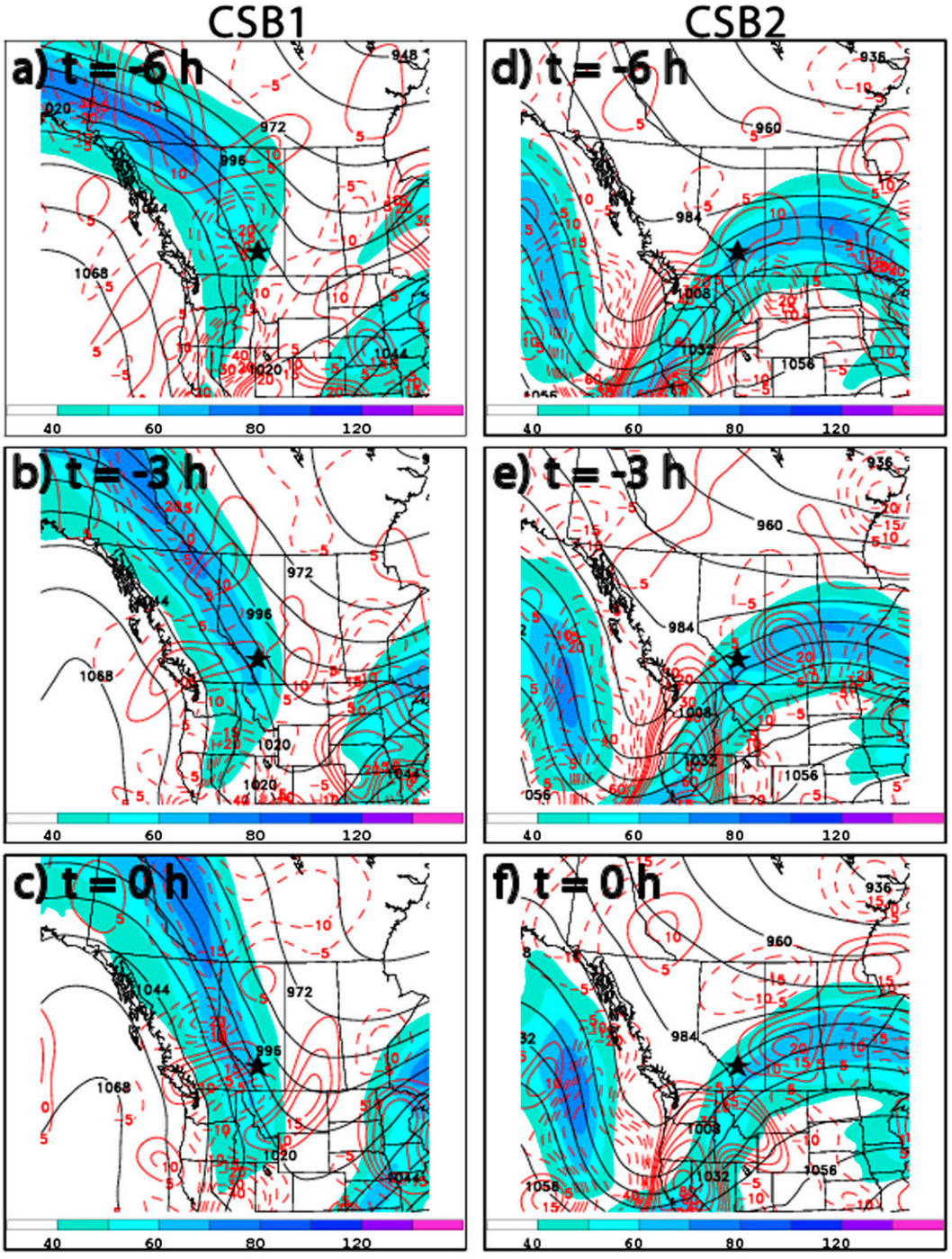

FIG. 4. For (left) CSB1 and (right) CSB2, NARR 250-hPa wind speeds (kt; shaded), 250-hPa geopotential height (dam; contours), and 500–250-hPa layer-averaged geostrophic absolute vorticity advection ($\times 10^{-10}$ s^{-2}; solid red for CVA, dashed red for AVA), at t = (a),(d) −6, (b),(e) −3, and (c),(f) 0 h. The approximate location of CYYC is marked with a black star.

a mesoscale anticyclonic circulation in the foothills of the U.S. Rockies.

In MGAS11, we concluded that frontogenesis served as a mesoscale ascent-focusing mechanism in the presence of synoptic-scale lift (primarily CVA), allowing for heavy banded precipitation given the release of various instabilities. Here, we find that CSB1 is marked by neutral **Q**-vector divergence in which lower-tropospheric CAA

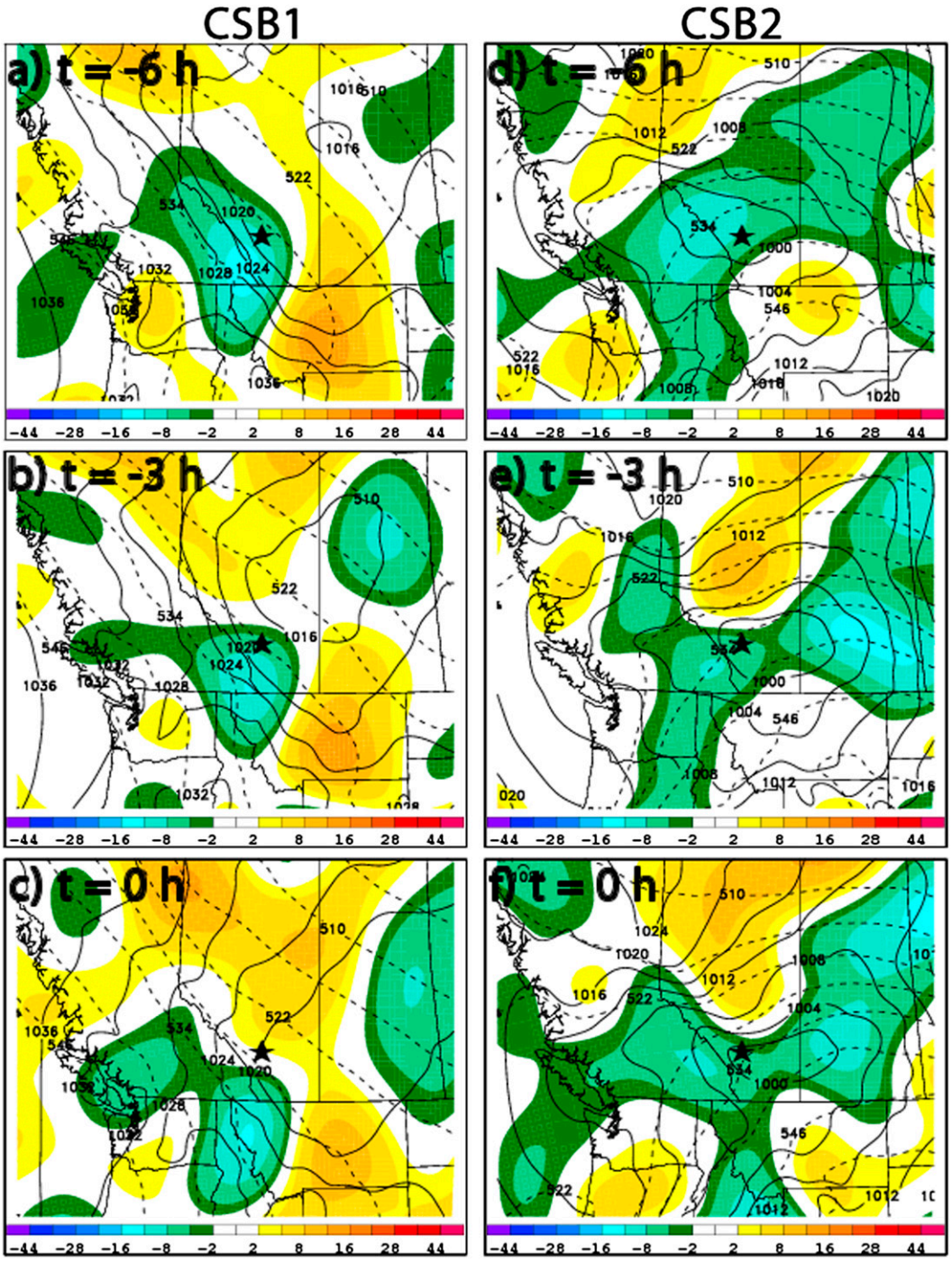

FIG. 5. As in Fig. 4, but for NARR sea level pressure (hPa; solid contours), 1000–500-hPa thickness (dam; dashed contours), and 850–250-hPa layer-averaged **Q**-vector divergence ($\times 10^{-18}$ K m^{-2} s^{-1}; shaded cool colors for convergence, warm colors for divergence).

cancels out CVA, while CSB2 is marked by **Q**-vector convergence in the presence of little to no temperature advection and CVA (Figs. 4 and 5). To gain more insight into ascent-forcing mechanisms, we now examine the frontogenesis in both cases.

Figure 6 shows strong lower-tropospheric frontogenesis over CYYC at $t = 0$ h for both CSB1 [approximately 50×10^{-2} K (100 km)$^{-1}$ (3 h)$^{-1}$] and CSB2 [approximately 100×10^{-2} K (100 km)$^{-1}$ (3 h)$^{-1}$]. For CSB1, the frontogenesis is oriented parallel to the higher terrain,

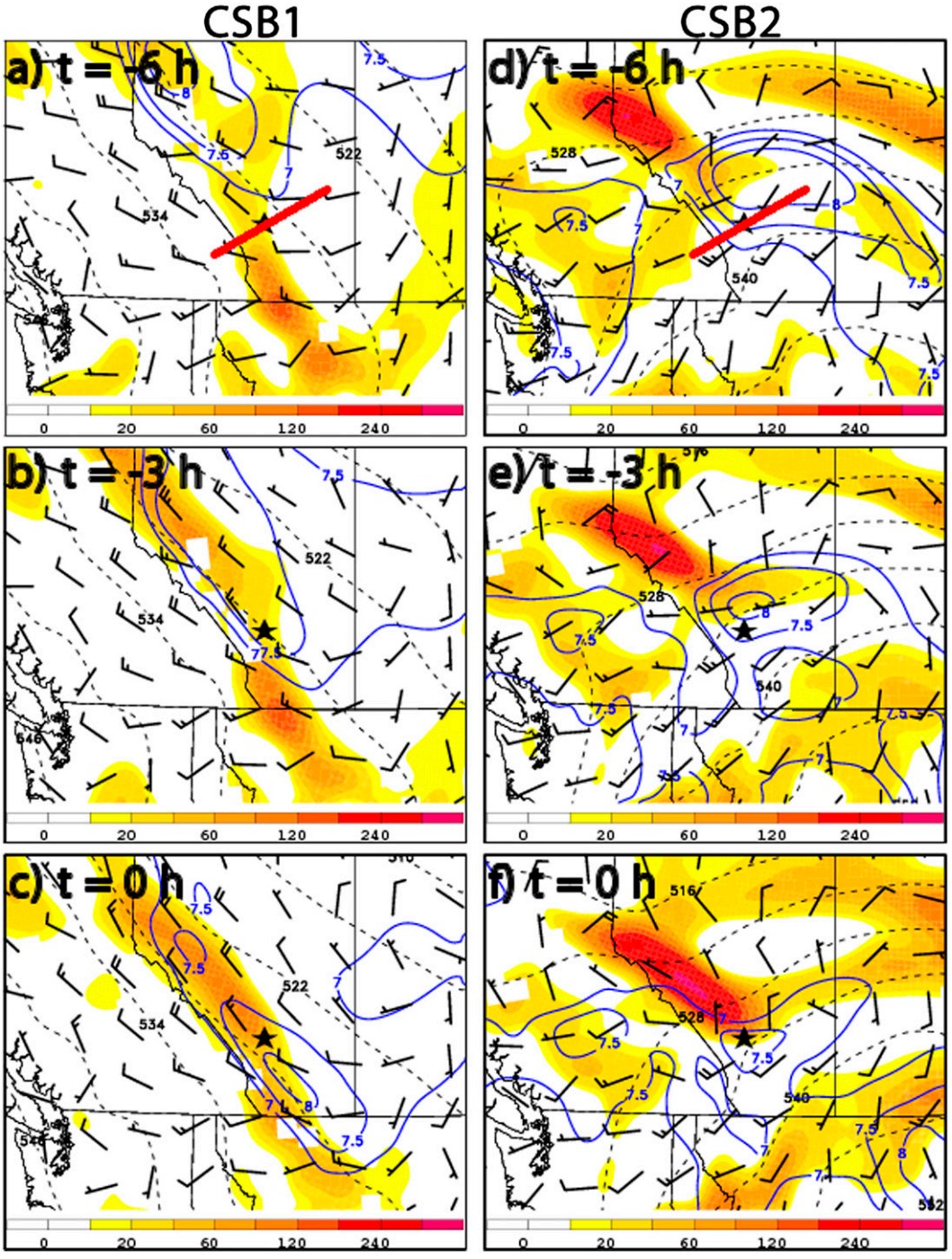

FIG. 6. As in Fig. 4, but for 850–700-hPa layer-averaged total frontogenesis [$\times 10^{-2}$ K (100 km)$^{-1}$ (3 h)$^{-1}$; shaded], 825–600-hPa lapse rate (°C km^{-1}; solid contours starting at 7 with an interval of 0.5), 1000–500-hPa thickness (dam; dashed), and 10-m wind (kt; barbs). A red line is placed in (a) and (d) to identify the cross-section area shown in Figs. 10 and 11.

stretching from northwestern Alberta southward to the Calgary region (Figs. 6a–c). At $t = -3$ h, steep lower-tropospheric lapse rates (>7.5°C km^{-1}) are observed over CYYC (Fig. 6b), suggestive of conditional instability (further discussed in section 4b). By $t = 0$ h (Fig. 6c), the frontogenesis intensifies over CYYC, and the lower-tropospheric lapse rates steepen. Given the lack of synoptic-scale lift at $t = 0$ h (Fig. 5c), we conclude that CSB1 is similar to the Schumacher et al. (2010) case in that frontogenesis is the primary ascent mechanism.

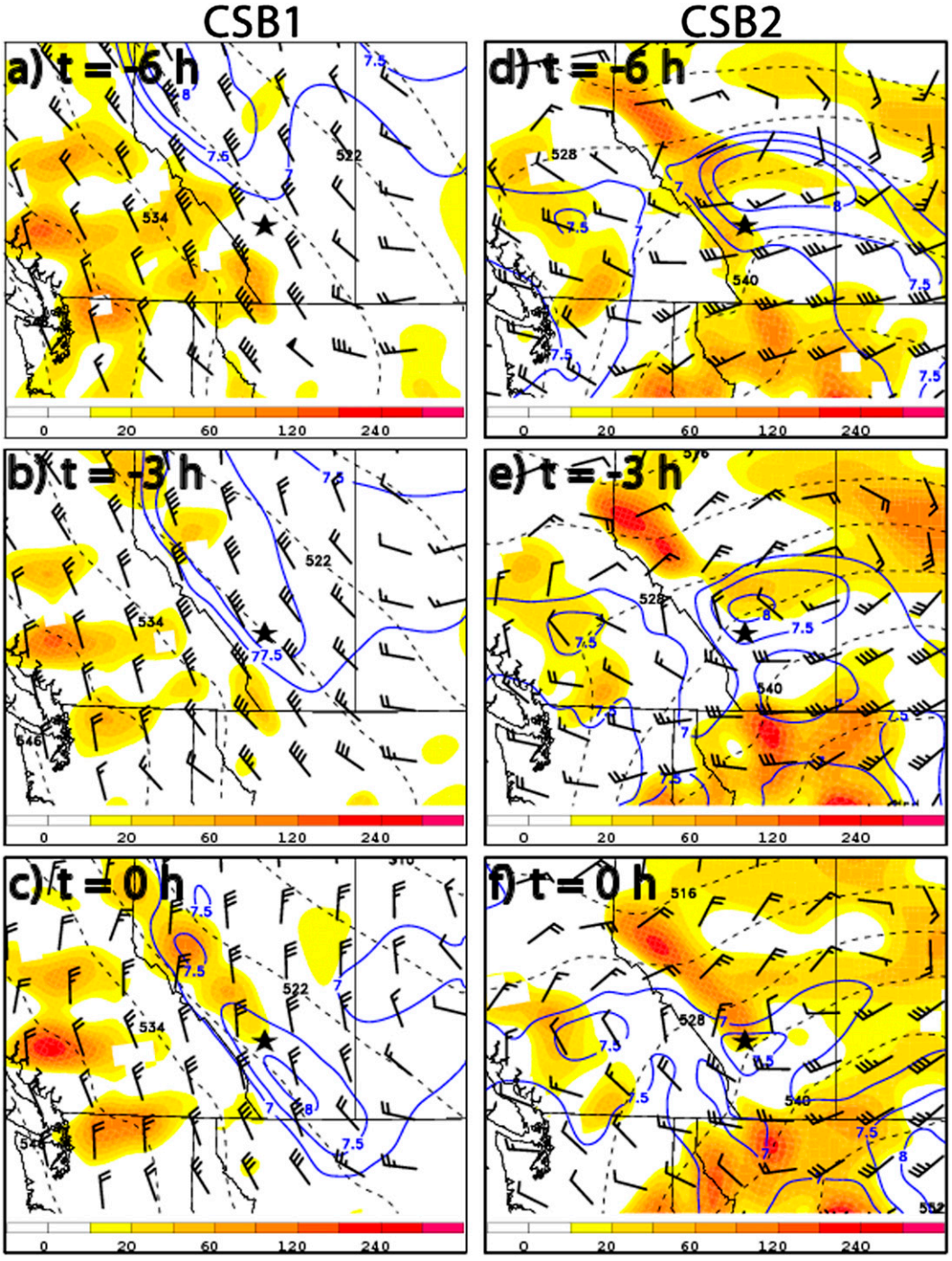

FIG. 7. As in Fig. 6, but for geostrophic frontogenesis.

The diagnostics for CSB2 show frontogenesis and lower-tropospheric lapse rates similar to those for CSB1 (Figs. 6e,f), although the orientation of the front is northeast–southwest, which likely explains the different orientations of the two snow bursts (Figs. 1 and 2). CSB2 also appears more similar to MGAS11, in which synoptic-scale lift and frontogenesis act in concert, than to Schumacher et al. (2010). We also note that despite the large area of frontogenesis northwest of CYYC (Fig. 6f), very little precipitation was observed in that area on radar (not shown). We suspect this is due to the area of **Q**-vector divergence (synoptic-scale forcing for descent) seen in Fig. 5f.

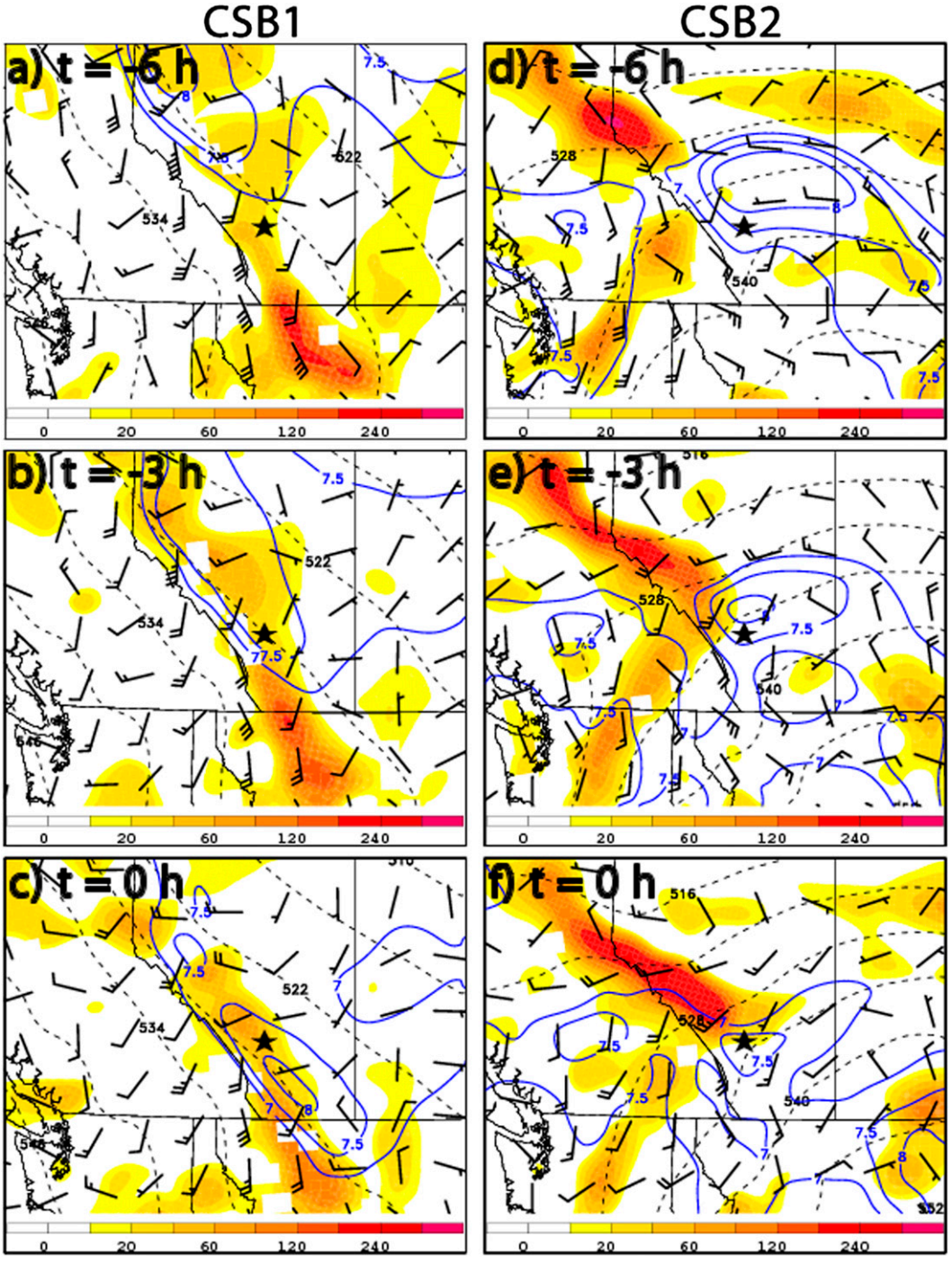

FIG. 8. As in Fig. 6, but for ageostrophic frontogenesis.

One aspect of snow bursts that to our knowledge has not been previously documented is the relative roles of geostrophic and ageostrophic frontogenesis. This distinction is particularly important in regions where complex terrain has an impact on the observed weather (e.g., Milrad et al. 2013). To that end, plots of 850–700-hPa geostrophic and ageostrophic frontogenesis are found in Figs. 7 and 8, respectively. At $t = 0$ h in CSB1, the total frontogenesis at CYYC is composed of mostly ageostrophic frontogenesis (Fig. 8c), as the geostrophic frontogenesis at CYYC throughout is essentially zero (Fig. 7c). This is also evidenced by nearly

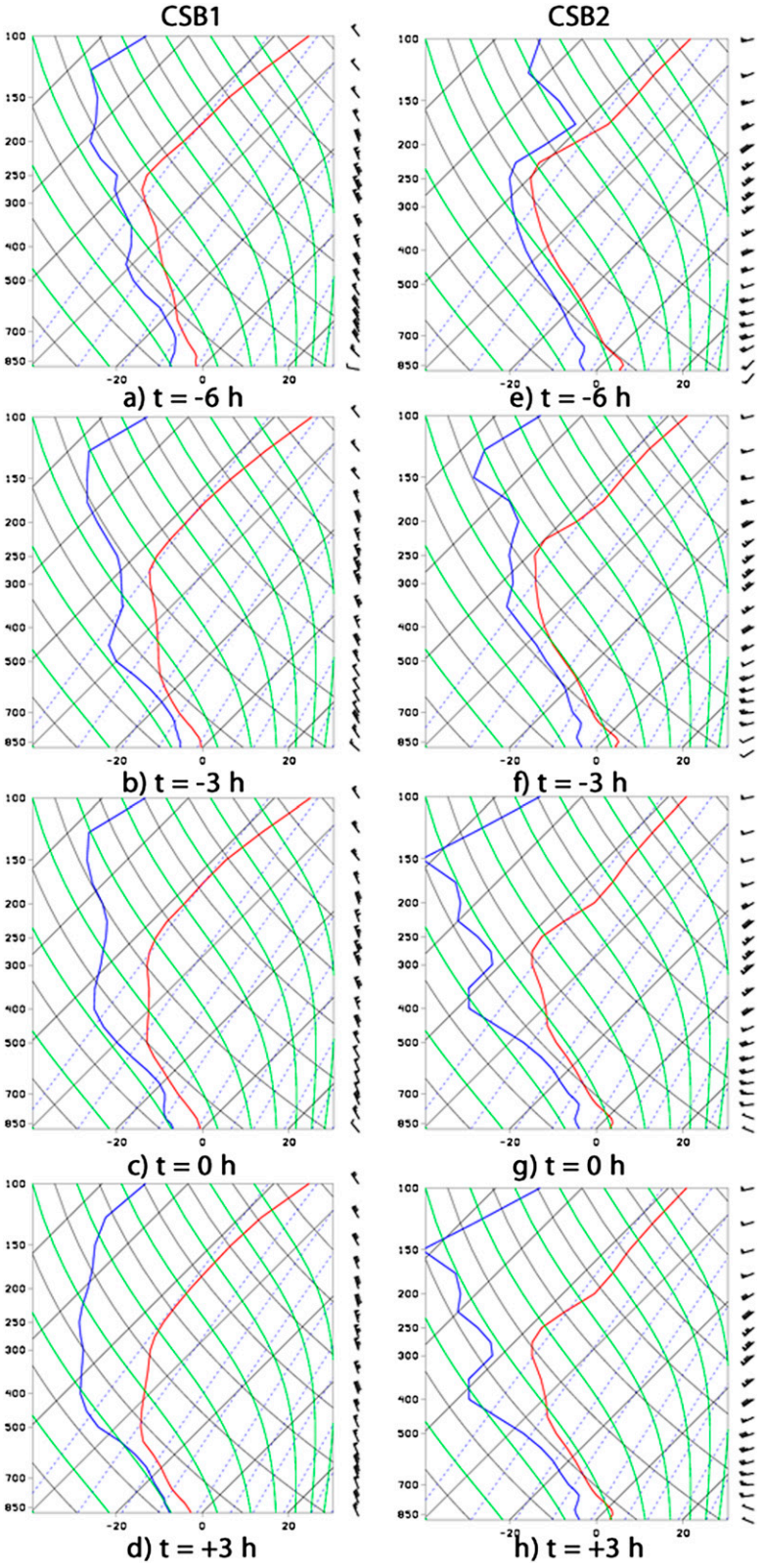

FIG. 9. NARR soundings for CYYC for (left) CSB1 and (right) CSB2, at t = (a),(e) −6, (b),(f) −3, (c),(g) 0, and (d),(h) +3 h. Temperature (dewpoint) is plotted in red (blue).

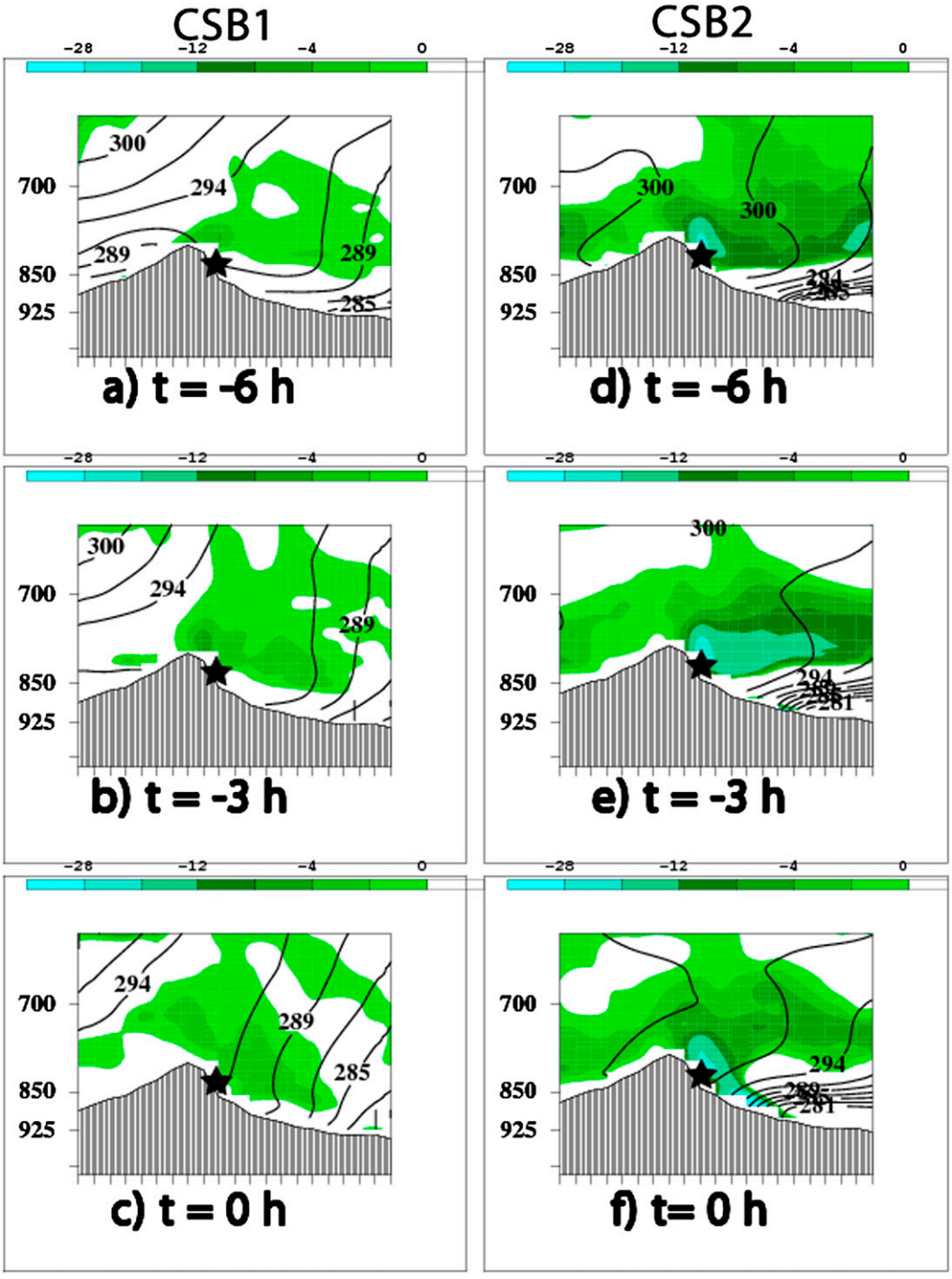

FIG. 10. Southwest–northeast cross sections from 48.64°N, 116.52°W to 53.64°N, 111.52°W, with CYYC located approximately at the halfway point of the cross section, and marked with a black star. A red line identifying the cross-section area is placed in Figs. 6a,d for CSB1 and CSB2, respectively. Plotted are the saturated equivalent geostrophic potential vorticity ($\times 10^{-7}$ m^2 s^{-1} K kg^{-1}; shaded for negative values) and equivalent potential temperature (K; solid contours).

uniform geostrophic wind magnitudes and directions throughout Alberta and British Columbia (Figs. 7c,f). In contrast, at $t = 0$ h, CSB2 is dominated by geostrophic frontogenesis (Fig. 7f), with only a small contribution from ageostrophic frontogenesis (Fig. 8f); this is also evidenced by the frontogenetical orientation of the geostrophic wind barbs near CYYC (Fig. 7f).

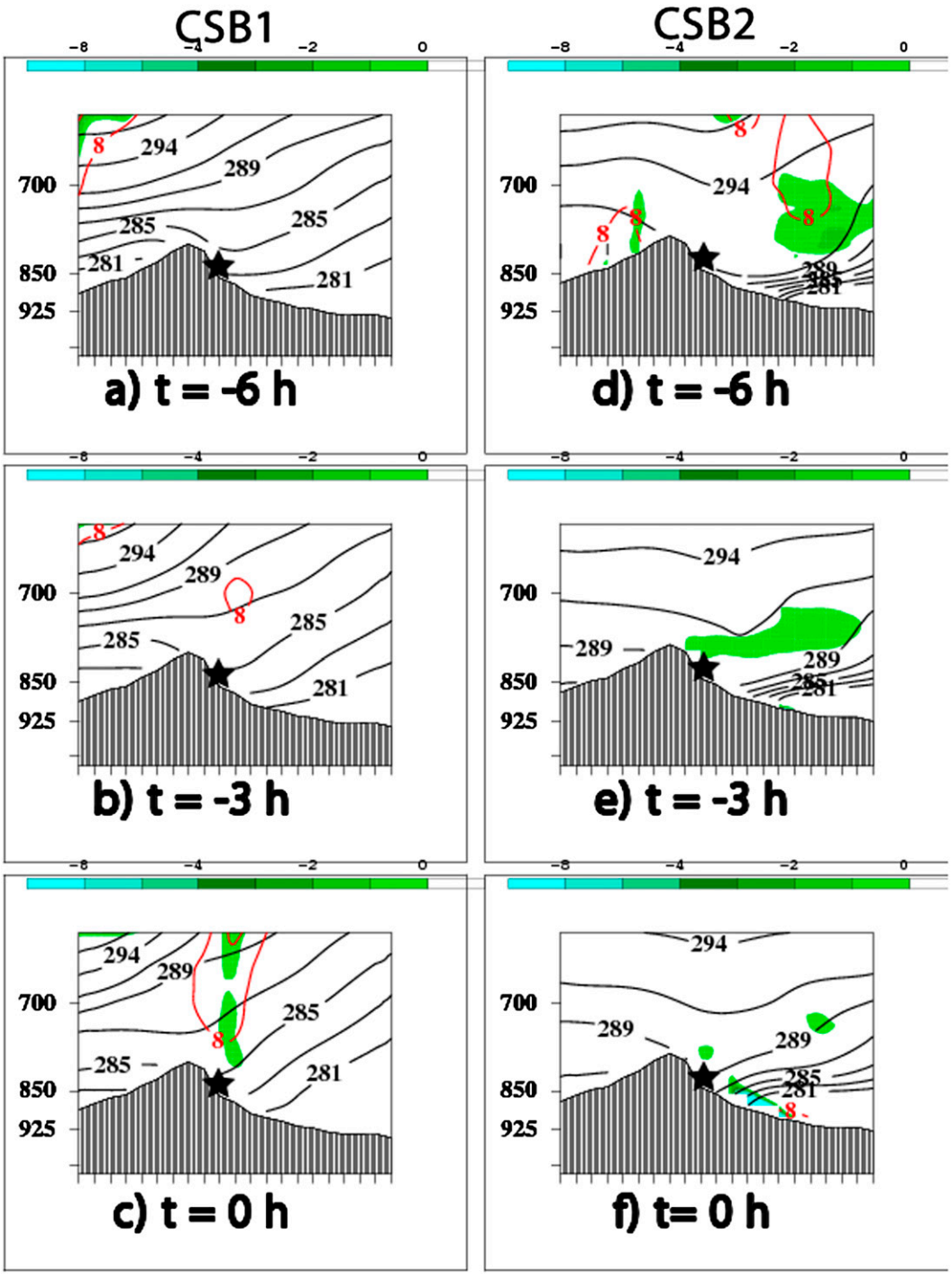

FIG. 11. As in Fig. 10, but for potential vorticity ($\times 10^{-7}$ m^2 s^{-1} K kg^{-1}; shaded for negative values), potential temperature (K; solid contours), and absolute vorticity ($\times 10^{-5}$ s^{-1}; solid red for positive values, dashed red for negative values; contoured at, e.g., 2, 5, 8, etc.). Both potential vorticity and absolute vorticity are calculated using the geostrophic wind, i.e., from the geopotential height field without filtering geostrophically unbalanced perturbations, following Schultz and Knox (2007).

Our results suggest the geostrophic frontogenesis and CVA in CSB2 (Fig. 7f) combine to result in **Q**-vector convergence and ascent (Fig. 5f), while the forcing for ascent in CSB1 is primarily due to mesoscale ageostrophic frontogenesis (Fig. 8c). To the latter point, the ageostrophic wind at $t = 0$ h is generally from the west (Fig. 8c), directed toward low pressure (the exiting 1016-hPa MSLP cyclone). This result mirrors the Schumacher et al. (2010)

case and results in the total near-surface wind being oriented parallel to the terrain (Fig. 6c), while the geostrophic wind is northerly (Fig. 7c). We therefore suggest that the downslope ageostrophic component contributes to the ageostrophic (Fig. 8c) and total (Fig. 6c) frontogenesis, which we explore further using numerical simulations (section 5). In contrast, during CSB2, the total (Fig. 6f) and geostrophic (Fig. 7f) winds are oriented similarly, reflective of a stronger MSLP cyclone (998 versus 1016 hPa) that is located closer to CYYC (Figs. 5c,f).

b. Instability

In the MGAS11 case, NARR soundings indicated the presence of a lower-tropospheric moist absolutely unstable layer (MAUL; Bryan and Fritsch 2000), up to 300 hPa deep at $t = 0$ h. In this study, CSB1 exhibits a shallow MAUL in the NARR data between 700 and 500 hPa at $t = -3$ and 0 h (Figs. 9b,c), if as in MGAS11, we consider the layer to be saturated with respect to ice. In contrast, a MAUL is not seen throughout the evolution of CSB2 (Figs. 9e–h), suggesting that a MAUL is not a necessary condition for a snow-burst event. We offer a more in-depth discussion of MAULs in snow bursts while discussing our numerical simulations (section 5b).

One thing that is seen in both CSB1 and CSB2 is conditional instability (Fig. 9) in the lowest 400 hPa, in accordance with the steep lapse rates observed in Figs. 6c,f. The release of conditional instability has also been found to play a role in previous studies on banded precipitation (e.g., Schultz and Knox 2007; Schumacher et al. 2010). Finally, the NARR wind profiles in both CSB1 and CSB2 suggest flow that is slightly downslope or parallel to the terrain (Fig. 9), which would seem to rule out many of the mechanisms discussed with respect to upslope banded convection by, for example, Kirschbaum and Durran (2005a,b).

Using southwest–northeast-oriented cross sections (marked with red lines in Figs. 6a,d) in Figs. 10 and 11, we now discuss various types of instability, as follows (for a more detailed description see Moore and Lambert 1993; Schultz and Schumacher 1999; Schultz and Knox 2007; Schumacher et al. 2010; MGAS11, and references therein):

- inertial instability—$\boldsymbol{\eta}_g < 0$, where $\boldsymbol{\eta}_g$ is the geostrophic absolute vorticity vector (s^{-1});
- convective (potential) instability (CI)—$d\theta_e/dz < 0$, where θ_e is equivalent potential temperature (K);
- dry symmetric instability—$PV_g < 0$, where PV_g is the geostrophic potential vorticity (PVU); and
- conditional symmetric instability (CSI)—$MPV_g^* < 0$, where MPV_g^* is the saturated equivalent geostrophic potential vorticity (PVU), explicitly defined by

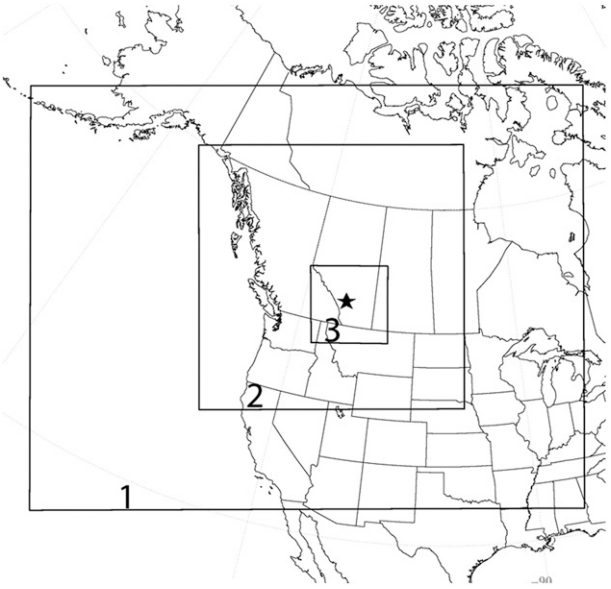

FIG. 12. Overview of the three model domains used in the WRF-ARW simulations. The horizontal grid spacings are 27, 9, and 3 km, for domains 1, 2, and 3, respectively. The approximate location of CYYC is marked with a black star.

TABLE 3. Design of the WRF-ARW, version 3.5, numerical model experiments, and comparison to the operational NAM. The domain locations are shown in Fig. 12. Here, GFDL refers to Geophysical Fluid Dynamics Laboratory.

Parameter	WRF-ARW	Operational NAM
Horizonal grid spacing (km)	27.0, 9.0, 3.0	12
Vertical levels	48, 48, 48	60
Time step (s)	108, 36, 12	27
Initial and boundary conditions	NARR	NAM
Cumulus convection	Kain (2004), Kain (2004), explicit	Janjić (1994)
Boundary layer	Yonsei University	Mellor–Yamada–Janjić
Surface layer	Monin–Obukhov	Janjić Eta Model
Microphysics	WSM six class	Ferrier
Land surface	Noah	Noah
Shortwave radiation	Dudhia (1989)	GFDL
Longwave radiation	Rapid radiative transfer	GFDL
Diffusion	Sixth-order monotonic (Knievel et al. 2007)	—
Scalar advection	Positive definite	Positive definite

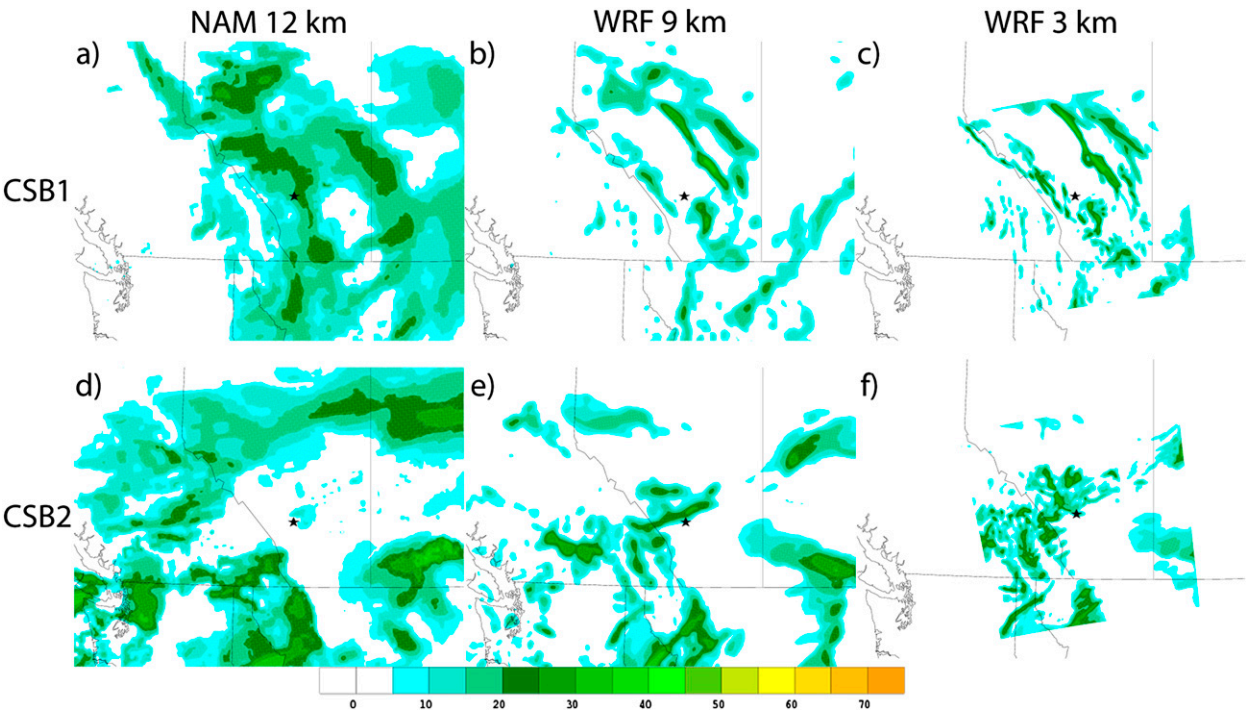

FIG. 13. Forecast composite radar reflectivity (dBZ; shaded), with all plots verifying at $t = 0$ h. For CSB1, from the (a) 12-km operational NAM initialized at 1200 UTC 3 Dec 2011, (b) 9-km WRF initialized at 1200 UTC 3 Dec 2011, and (c) 3-km WRF initialized at 1200 UTC 3 Dec 2011. For CSB2, is from the (d) 12-km operational NAM initialized at 1200 UTC 9 Jan 2013, (e) 9-km WRF initialized at 1500 UTC 9 Jan 2013, and (f) 3-km WRF initialized at 1500 UTC 9 Jan 2013.

$$\mathrm{MPV}_g^* = g\boldsymbol{\eta}_g \cdot \nabla\theta_e^*, \tag{3}$$

where g is gravity, $\boldsymbol{\eta}_g$ is the three-dimensional geostrophic absolute vorticity vector, ∇ is the gradient operator in x and y, and θ_e^* is the saturated equivalent potential temperature. Schultz and Schumacher (1999) pointed out that MPV_g^* is not very sensitive to the orientation of the cross section, unlike geostrophic absolute momentum M_g surfaces. For inertial instability and dry symmetric instability, Schultz and Knox (2007) discussed in detail whether to perform the calculation using the geostrophic wind or the total wind. Because Schultz and Knox (2007) and Schumacher et al. (2010) found that using the geostrophic wind in both calculations produced more robust results, we follow that methodology here.

Novak et al. (2004, 2006, 2008, 2009, 2010) found that conditional, inertial, and moist symmetric instabilities were all possibilities in heavy snowbands within extratropical cyclones and that conditional instability existed 30% of the time before the band formed, something that we see in CSB1 and CSB2 (section 4a; Figs. 6 and 9). However, as Schumacher et al. (2010) pointed out, bands within the cold conveyor belt of extratropical cyclones form in completely saturated environments while snow bursts often form in near- or subsaturated environments. Emanuel (1983), Moore and Lambert (1993), and Schultz and Schumacher (1999) provide good overviews of the interplay between CI and CSI. They found that when both CI and CSI are present, CI tends to dominate over time. However, situations can exist in which both CSI and CI are acting together (convective-symmetric instability), or CSI actually precedes CI even if CI eventually dominates over time (Schultz and Schumacher 1999). In MGAS11, we generally found that both CI and CSI were present during the snow bursts, but we did not attempt to determine which instability was dominant, and we follow that strategy here. Finally, it is important to stress that any instability must be released by an ascent mechanism (e.g., Schultz and Knox 2007; Schumacher et al. 2010), which are primarily ageostrophic and geostrophic frontogenesis for CSB1 and CSB2, respectively.

For CSB1, Fig. 10 shows a large region of lower-tropospheric CSI (shading) starting at $t = -6$ h (Fig. 10a). While the atmosphere over CYYC is convectively stable at $t = -6$ h (Fig. 10a), it becomes less so at $t = -3$ and 0 h (Figs. 10b,c), when the θ_e isentropes are essentially upright. In CSB2, CSI is also present over CYYC starting at $t = -6$ h (Fig. 10d) and becomes stronger by $t = -3$ and 0 h (Figs. 10e,f). Weak convective stability is also evident throughout; by $t = 0$ h (Fig. 10f), there is evidence

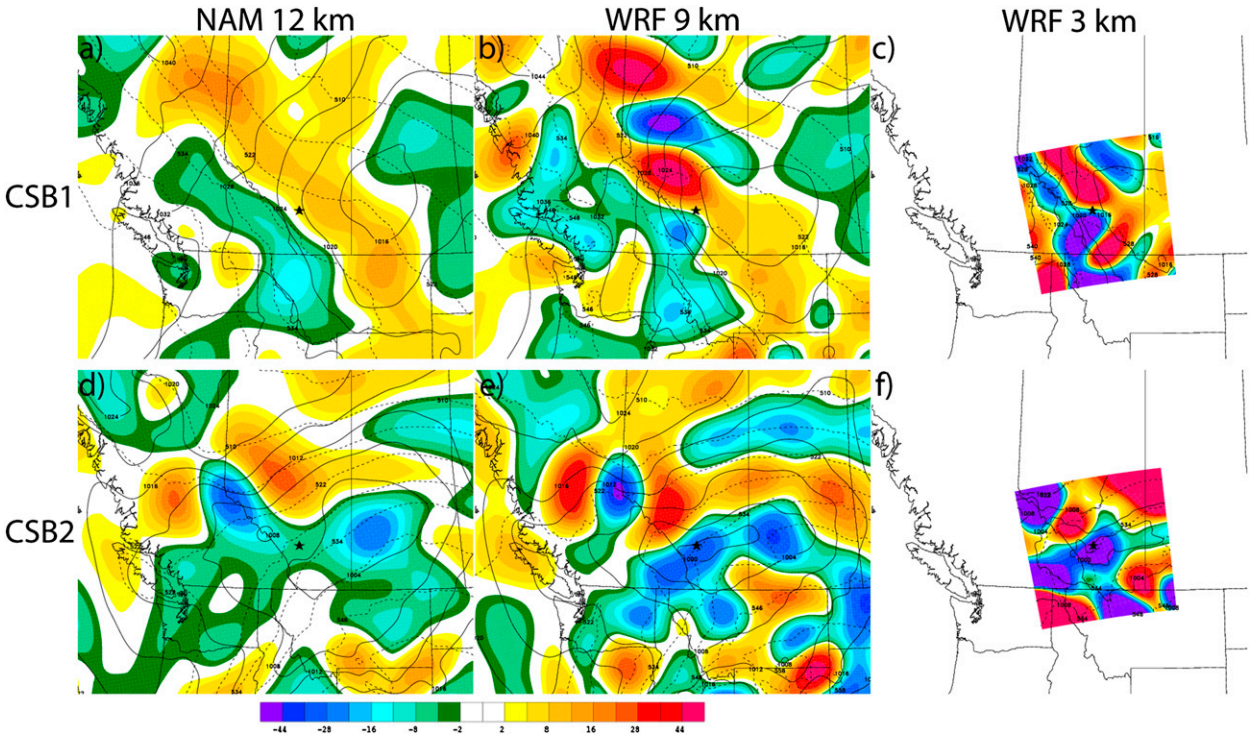

FIG. 14. As in Fig. 13, but for sea level pressure (hPa; solid contours), 1000–500-hPa thickness (dam; dashed contours), and 850–250-hPa layer-averaged **Q**-vector divergence ($\times 10^{-18}$ K m^{-2} s^{-1}; shaded cool colors for convergence, warm colors for divergence). The approximate location of CYYC is marked with a black star.

of CI, as θ_e decreases with height just above the surface. These results mirror those of MGAS11; both CSB1 and CSB2 are marked by an environment where CSI precedes CI, but CI dominates over time (e.g., Schultz and Schumacher 1999).

Both Schultz and Knox (2007) and Schumacher et al. (2010) found that the release of CSI likely did not play a major role in generating convective snowbands in the foothills of the Rockies because the atmosphere was far from saturated; however, both inertial and dry symmetric instability were judged to be important. Since Calgary is located in relatively high terrain in the foothills of the Rockies, Fig. 11 explores the possibility of inertial and/or dry symmetric instability. Unlike in Schultz and Knox (2007) and Schumacher et al. (2010), there is no evidence of inertial instability (negative absolute vorticity) in either CSB1 or CSB2 in the NARR; we explore this further using numerical simulations (section 5c). Dry symmetric instability ($PV_g < 0$) is evident over CYYC at $t = 0$ h in both CSB1 (Fig. 11c) and CSB2 (Fig. 11f). The question of whether dry symmetric instability or CSI is appropriate to use is an important one; in MGAS11, we judged it to be CSI because the lower troposphere was saturated with respect to ice. In CSB1 and CSB2, NARR soundings at $t = 0$ h (Figs. 9c,g) underestimate the saturation near the surface compared to observations (Tables 1 and 2, Fig. 3). However, the midtroposphere is saturated with respect to ice, leaving us to explore this issue in more depth using numerical simulations (section 5c). It is important to realize, however, that that CI is also occurring at $t = 0$ h (Fig. 10), which tends to dominate CSI when both are present (e.g., Schultz and Schumacher 1999).

5. Model forecast evaluation and numerical simulations

a. *Overview*

Version 3.5 of the WRF-ARW was run using three nested domains at grid spacings of 27, 9, and 3 km, centered on CYYC (Fig. 12). The model settings (e.g., 48 vertical levels; Table 3) were very similar to those used by Schumacher et al. (2010), although we did not run a 1-km simulation. The 3-km domain includes explicit (not parameterized) convection, however, which Schumacher et al. (2010) found to be crucial to the model's ability to reproduce convective snowbands. The model was initialized 12 h prior to $t = 0$ h for each event (1200 UTC 3 December 2011 for CSB1 and 1500 UTC 9 January 2013 for CSB2), and the NARR was used to initialize the

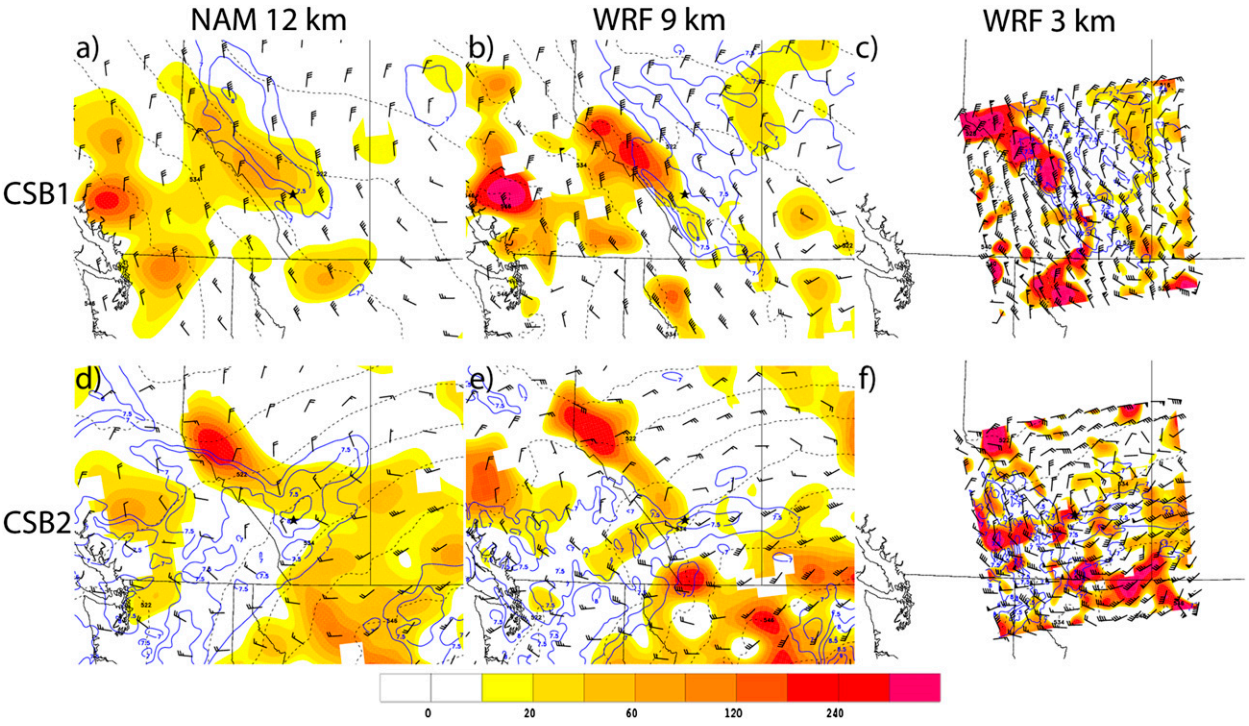

FIG. 15. As in Fig. 13, but for 850–700-hPa layer-averaged geostrophic frontogenesis [$\times 10^{-2}$ K (100 km)$^{-1}$ (3 h)$^{-1}$; shaded], 825–600-hPa lapse rate (°C km^{-1}; solid contours starting at 7 with an interval of 0.5), 1000–500-hPa thickness (dam; dashed), and 825-hPa geostrophic wind (kt; barbs).

model and for lateral boundary conditions, updated every 3 h.

For the remainder of section 5, we analyze the performance of the operational NAM [as was also done by Schumacher et al. (2010)] run initialized at the time closest to our WRF runs (1200 UTC 3 December 2011 for CSB1 and 1200 UTC 9 January 2013 for CSB2) and the two inner WRF domains (9 and 3 km) for both snow bursts. The dynamic and thermodynamic analyses used are similar to those presented in section 4.

b. *Lift*

Figure 13a shows that at $t = 0$ h, the NAM generates a northwest–southeast-oriented snow burst, similar to the radar appearance of CSB1 (Fig. 1). In contrast, the 9-km (Fig. 13b) and 3-km (Fig. 13c) WRF simulations do not generate an organized snow burst over CYYC, although the 3-km run does hint at a northwest–southeast-oriented band to the west of Calgary that moved through CYYC 1 h earlier (not shown). The misplaced location and timing have been similarly found in previous studies with explicit convection simulations (Schumacher et al. 2010 and references therein). Figures 13d–f show a completely different result for CSB2, as the NAM does not forecast a northeast–southwest-oriented snow burst at all, while both the 9- and 3-km WRF runs simulated the appearance and timing of CSB2 (Fig. 2). The NAM forecast issues with CSB2 are ostensibly not related to resolution, as the 27-km WRF also simulated the snow burst at the same time and location (not shown).

In terms of the synoptic-scale dynamics for CSB1, both the NAM and WRF runs produce results consistent with the NARR. Figures 14a–c show that the NAM, WRF 9-km, and WRF 3-km simulations all place a 1016-hPa cyclone to the east-northeast of CYYC, although the WRF runs are slightly faster, perhaps explaining the timing of the simulated convective snowband by the 3-km run. CYYC is generally in an area of neutral to slightly positive **Q**-vector divergence under geostrophic CAA, concurring with the NARR results. In CSB2, the NAM underestimates the intensity of the MSLP cyclone (1004 hPa; Fig. 14d) compared to the NARR (996 hPa; Fig. 5f) and WRF (1000 hPa; Figs. 14e,f). The **Q**-vector convergence in the NAM (Fig. 14e) is also weaker than in the WRF 9-km simulation (Fig. 14f), suggesting that the NAM did not simulate the ascent correctly; we explore this point further below.

In section 4a, we showed that the forcing for ascent in CSB1 is caused by ageostrophic frontogenesis, while in CSB2 it is related to geostrophic frontogenesis and CVA

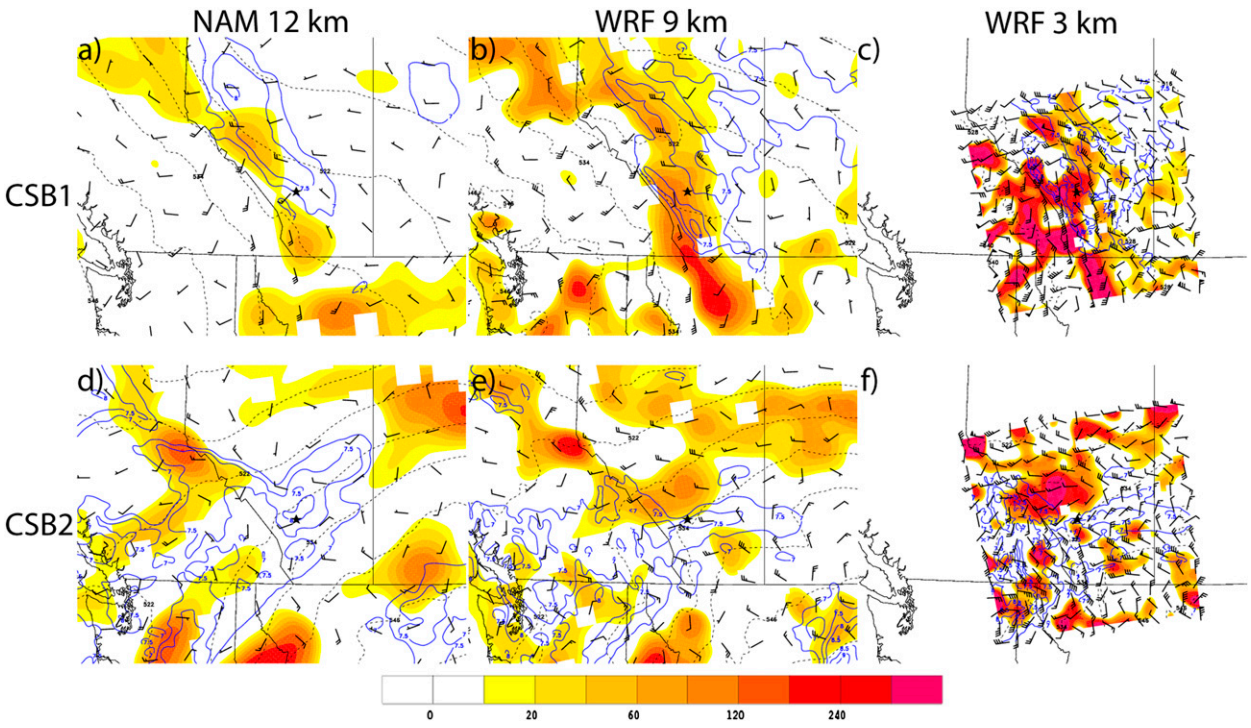

FIG. 16. As in Fig. 13, but for ageostrophic frontogenesis.

(both associated with **Q**-vector convergence). Our numerical simulations support these assertions and show that the NAM did not correctly forecast the frontogenesis in both cases. For CSB1, Fig. 15a shows that the NAM overpredicted the amount of geostrophic frontogenesis at CYYC, although it did correctly simulate conditionally unstable ($>7°C\,km^{-1}$) lower-tropospheric lapse rates in the region. Both the WRF 9- and 3-km simulations (Figs. 15b,c) are similar to the NARR (Fig. 7c) in that the main area of geostrophic frontogenesis is located to the northwest of where CSB1 occurred. The NAM underpredicts ageostrophic frontogenesis for CSB1 (Fig. 15a), while both WRF runs show strong [$>80 \times 10^{-2}$ K $(100\,km)^{-1}$] ageostrophic frontogenesis oriented northwest–southeast through CYYC, which matches the NARR (Fig. 8c). To that end, we note that higher-resolution models are capable of simulating tighter gradients, resulting in higher magnitudes of certain fields such as frontogenesis, vorticity, etc., despite the use of smoothing algorithms. Both WRF simulations also forecast steep lapse rates in the vicinity of CYYC, supporting the NARR results and suggesting conditional instability (discussed further in section 5c).

For CSB2, the NAM simulates an area of geostrophic frontogenesis (Fig. 15d) that is located farther to the north and northeast than in the NARR (Fig. 7f) and both WRF simulations (Figs. 15e,f). This likely explains why **Q**-vector convergence is weaker in the NAM (Fig. 14d) than in the NARR (Fig. 5f) and WRF (Figs. 14e,f). All models accurately show conditional instability ($>7.5°C\,km^{-1}$ lower-tropospheric lapse rates) in the vicinity of CSB2, but the WRF simulations show only a narrow band of conditional instability (Figs. 15e,f), collocated with the simulated snow burst (Figs. 13e,f). Finally, the NAM and WRF simulations all concur with the NARR (Fig. 8f) in showing little to no ageostrophic frontogenesis in the location of CSB2 (Figs. 16d,f).

In summary, Figs. 13–16 suggest that the WRF simulations outperform the NAM with respect to CSB2, both in terms of simulated reflectivity and dynamical forcing for ascent. Results for CSB1, however, are less clear, as the NAM did not forecast any ascent, in stark contrast to the WRF simulations.

Figure 17 shows cross sections taken along the red lines visible in Figs. 6a and 6d for CSB1 and CSB2, respectively. It is obvious that for CSB1 the NAM did not forecast any ascent near CYYC (Fig. 17a), questioning the validity of the NAM forecast reflectivity (Fig. 13a). Meanwhile, both the WRF 9- and 3-km simulations show ascent near CYYC in the 800–650-hPa level in association with lower-tropospheric frontogenesis (Figs. 17b,c). Note that the isentropes slope downward in the higher terrain west of CYYC, while upgliding is observed in the vicinity of CYYC; this issue is further discussed within

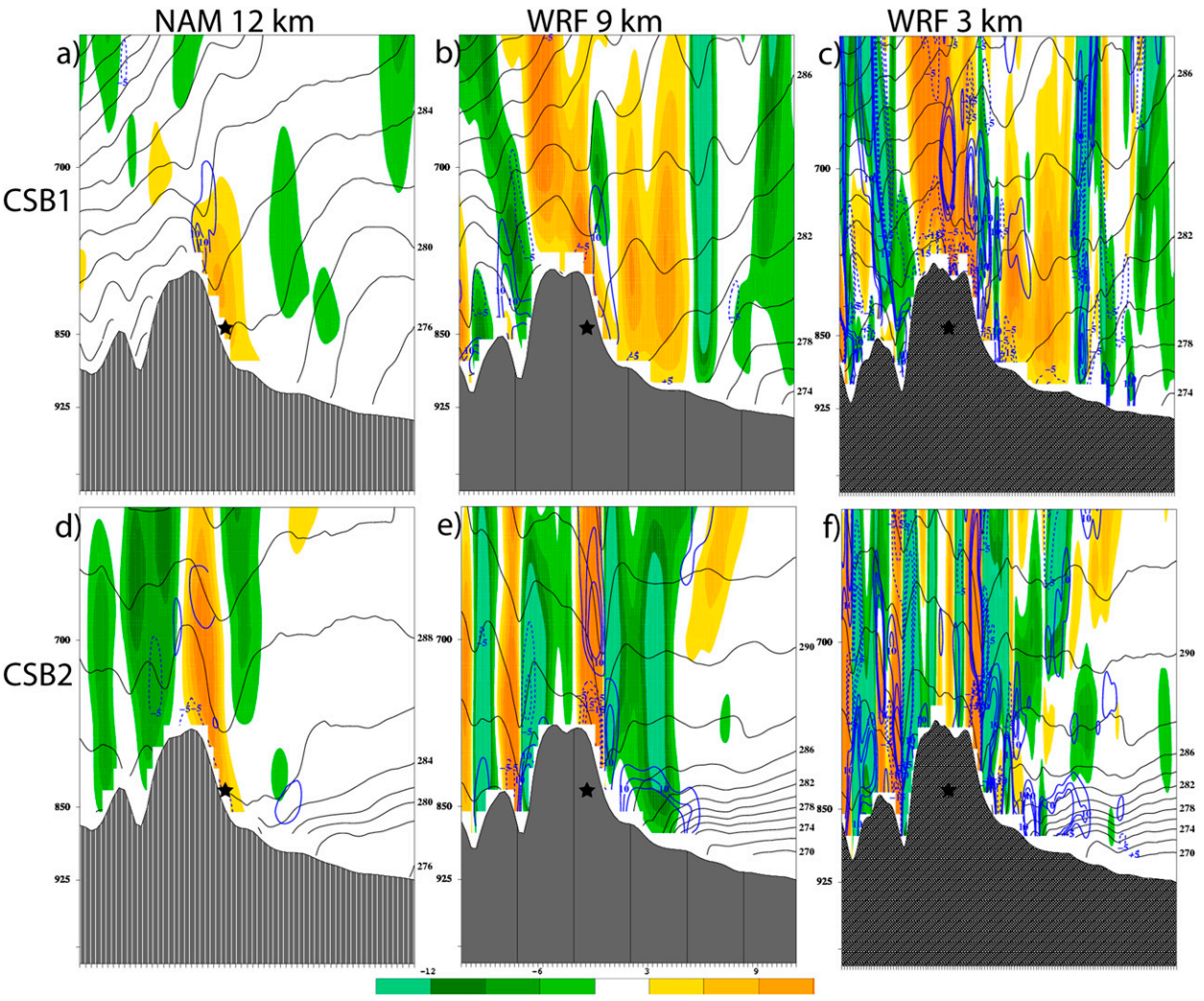

FIG. 17. As in Fig. 13, but for southwest–northeast cross sections from 48.64°N, 116.52°W to 53.64°N, 111.52°W, with CYYC located approximately at the halfway point of the cross section, and marked with a black star. Red lines identifying the cross section areas are placed in Figs. 6a,d for CSB1 and CSB2, respectively. Plotted are omega ($\times 10^{-2}$ mb s^{-1}; shaded cool colors for ascent, warm colors for descent), potential temperature (K; solid black contours), and total frontogenesis [K (100 km)$^{-1}$ (3 h)$^{-1}$; blue contours, solid for positive values, dashed for negative values].

the context of released instabilities in section 5c. For CSB2, the NAM does not forecast the horizontal and vertical extent of the ascent (Fig. 17d), while both the WRF 9- and 3-km runs (Figs. 17e,f) show deep-layer ascent (and associated upgliding) in the presence of lower-tropospheric frontogenesis over CYYC.

We can conclude to this point that the NAM simply did not correctly simulate the dynamics in CSB2 and therefore does not simulate a snow burst (Fig. 13d). In CSB1, however, the NAM forecast reflectivity (Fig. 13a) is misleading, as the model forecasts a snowband in nearly the same area as CSB1 while inaccurately forecasting the forcing for ascent (Figs. 14a, 15a, and 16a) and the ascent itself (Fig. 17a). We now attempt to shed more light on various instabilities in the NAM and WRF simulations.

c. *Instability*

For both cases, Fig. 18 supports the aforementioned conditional instability at CYYC. The NAM and WRF simulations clearly show an environment characterized by some CAPE and steep lower-tropospheric lapse rates, similar to the convective snowbands of Schumacher et al. (2010). It is also clear from the WRF simulations (Figs. 18e,f) that the NARR underestimates the degree of saturation in CSB2 (Fig. 8).

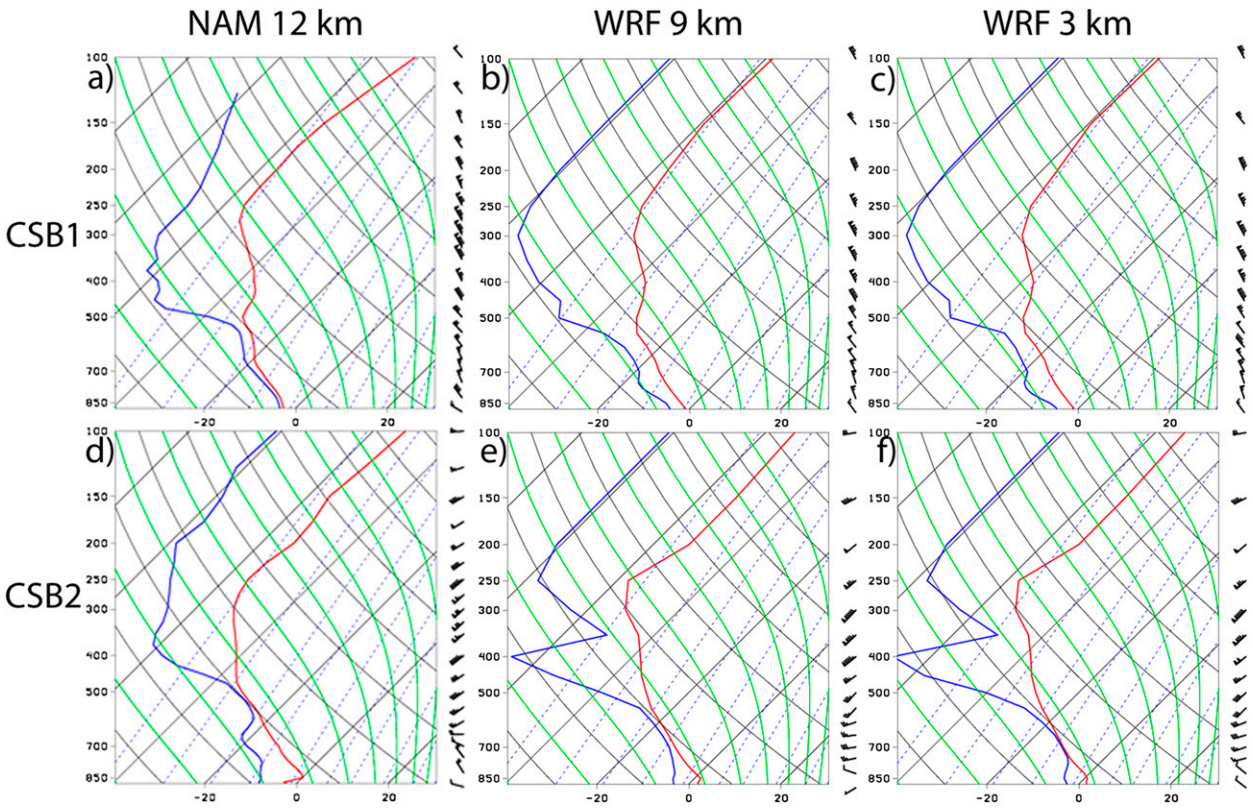

FIG. 18. As in Fig. 13, but for soundings at CYYC. Temperature (dewpoint) is plotted in red (blue).

In CSB1, the NAM does simulate a MAUL in the lowest 200 hPa (Fig. 18a), but neither of the WRF simulations does (Figs. 18b,c). This further brings into question whether MAULs are artifacts of the model (R. Schumacher 2013, personal communication) or only appear in some cases of snow bursts (e.g., MGAS11). Interestingly, both WRF runs show a shallow MAUL for CSB2 (Figs. 18e,f), while the NAM does not (Fig. 18d). We should note that the dynamics of CSB2 (geostrophic frontogenesis, **Q**-vector convergence) are more similar to the MGAS11 cases, while CSB1 resembles the Schumacher et al. (2010) case. It is therefore possible that MAULs are more likely with ''traditional'' snow-burst cases (e.g., MGAS11, CSB2), but not cases (e.g., CSB1) that lack saturation and occur where the complex terrain plays a major role. More snow-burst cases need to be examined to assess the legitimacy of the MAUL, both in saturated and subsaturated situations.

Figures 19a–c show that the NAM and WRF all simulated large regions of CSI near CYYC at $t = 0$ h, corresponding with the NARR results. Additionally, the isentropes are nearly vertical, signifying the presence of CI. Since the WRF soundings (Figs. 18b,c) show subsaturation throughout the column, CSI is less important, as in the Schumacher et al. (2010) case. The results for CSB2 show similar structures to the NARR (CSI and CI; Figs. 19d,f); given the saturation seen in Figs. 18e,f, we can conclude that the release of CSI and CI are important mechanisms in the production of CSB2. This result again relates CSB2 more to MGAS11 than to Schumacher et al. (2010).

Finally, in section 4b, we found no evidence of inertial instability in the NARR for both cases. However, as Schumacher et al. (2010) pointed out, the resolution of the reanalysis versus the WRF simulations and the explicit convection in the 3-km WRF simulation are important here, particularly within the context of the region's complex terrain. For CSB1, while the NAM forecasts dry symmetric instability (Fig. 20a), there is no evidence of inertial instability. The WRF simulates inertial and dry symmetric instability near CYYC in the 800–700-hPa layer (Figs. 20b,c), coinciding with the simulated ascent (Figs. 17b,c). Schumacher et al. (2010, and references therein) referred to such areas as potential vorticity PV banners located just downstream of high terrain and related them to a northwest–southwest-oriented jet streak also observed in CSB1 (Figs. 4c and 20b). We therefore echo Schumacher et al. (2010)

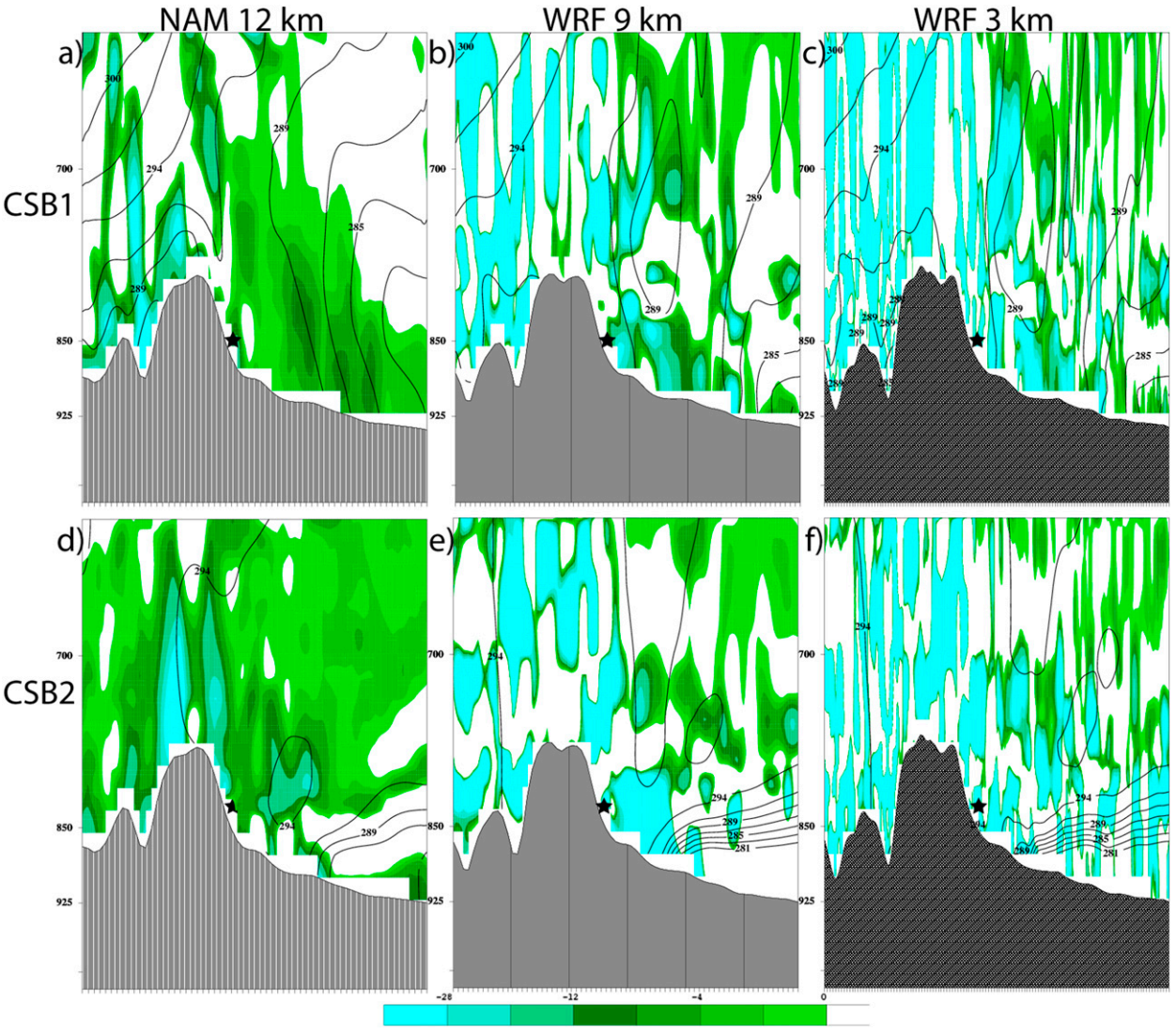

FIG. 19. As in Fig. 17, but for saturated equivalent geostrophic potential vorticity ($\times 10^{-7}$ m^2 s^{-1} K kg^{-1}; shaded for negative values) and equivalent potential temperature (K; solid contours).

in summary of the mechanisms for CSB1: a convective snowband (snow burst) formed downstream of high terrain in which frontogenesis (here, primarily ageostrophic frontogenesis) helps to release conditional, dry symmetric, and inertial instability, wherein the presence of inertial instability is related to fast flow over terrain associated with a mid- to upper-tropospheric jet streak and a PV banner.

In CSB2, there is some inertial instability in the WRF 3-km simulation located over the higher terrain and to the northeast of CYYC (Fig. 20f). However, we do not consider inertial instability to be a major factor in CSB2, because neither the WRF 27-km (not shown) nor the 9-km (Fig. 20e) simulation shows any evidence of it, and yet both simulate the snow burst at the correct time and location (Fig. 13e). As such, we summarize the mechanisms that produce CSB2 to be similar to MGAS11: (geostrophic) frontogenesis ahead of a midtropospheric trough results in the release of conditional instability, CI, and CSI, with CI dominating CSI over time (e.g., Schultz and Schumacher 1999).

6. Conclusions and future work

This study complements the work of Schumacher et al. (2010) and MGAS11, examining two cases (CSB1 and CSB2) of snow bursts that impacted the Calgary, Alberta (CYYC), region in December 2011 and January 2013, respectively. As in DeVoir (2004), Pettegrew et al. (2009), Schumacher et al. (2010), and MGAS11, CSB1

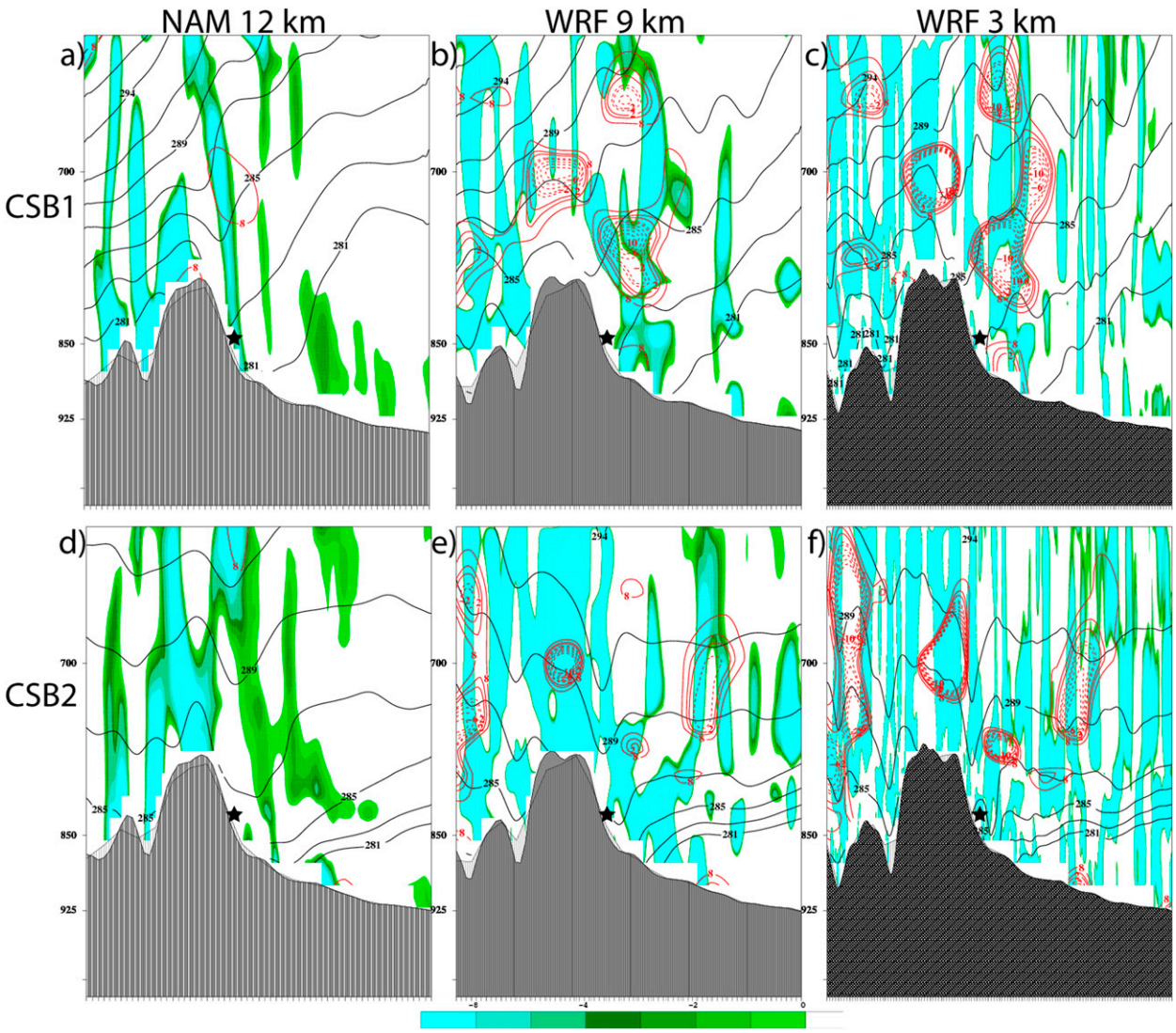

FIG. 20. As in Fig. 17, but for potential vorticity ($\times 10^{-7}\,\mathrm{m^2\,s^{-1}\,K\,kg^{-1}}$; shaded for negative values), potential temperature (K; solid contours), and absolute vorticity ($\times 10^{-5}\,\mathrm{s^{-1}}$; solid red for positive values, dashed red for negative values, contoured at, e.g., 2, 5, 8, etc.). Both potential vorticity and absolute vorticity are calculated as detailed in Fig. 11.

and CSB2 are high-impact events with relatively small snow accumulations that feature brief periods of moderate or heavy snow, low visibilities, and strong gusty winds (Tables 1 and 2, Figs. 1–3).

Through the use of reanalysis (NARR) data, an operational forecast model (NAM), and high-resolution convection-explicit WRF simulations, we find that CSB1 and CSB2, while similar in appearance, are produced by very different mechanisms. CSB1 occurs slightly downstream of a strong mid- to upper-tropospheric northwest–southeast-oriented jet streak, in the presence of neutral to slightly positive **Q**-vector divergence, and ageostrophic frontogenesis oriented parallel to the snow burst. Conditional, dry symmetric, and inertial instability are all released by the ageostrophic frontogenesis, which serves as the primary ascent mechanism. While the conditional instability and total frontogenesis are consistent with MGAS11, CSB1 more closely resembles Schumacher et al. (2010), in which fast flow over high terrain (PV banner) and the release of the aforementioned instabilities resulted in the appearance of convective snowbands.

In contrast, CSB2 more closely resembles MGAS11, in which **Q**-vector convergence (caused by CVA and geostrophic frontogenesis) releases conditional instability, CI, and CSI, in a more saturated environment than CSB1. Synthesizing our results with those of DeVoir (2004), Pettegrew et al. (2009), Schumacher et al. (2010), and MGAS11, we suggest that frontogenesis associated

with the approach and passage of a cold front and the release of conditional instability are observed in all cases studied to this point. However, the location (e.g., regions of elevated terrain) and degree of saturation vary among cases, which results in different responsible ascent-forcing mechanisms and instabilities.

One thing that is clear is that high-resolution convection-explicit numerical simulations are capable of reproducing the dynamics and in large part the structure of snow bursts, if not always the exact timing and location [e.g., CSB1; Schumacher et al. (2010)]. More cases and preferably a climatology of these cases need to be studied in order to gain a comprehensive understanding of the dynamic and thermodynamic mechanisms. To that end, remaining substantive research questions and avenues for future work include the following:

- Are particular dynamical mechanisms (e.g., synoptic-scale QG ascent, ageostrophic and geostrophic frontogenesis) necessary or more prevalent for snow bursts in certain regions of North America?
- With what frequency are MAULs observed in snow-burst events?
- Does inertial instability only play a role in snow-burst events near areas of high terrain?
- Does a snow burst in which the atmosphere is saturated require the release of both CSI and CI?
- Model forecast evaluation questions include the following:
  - How do model convective parameterizations relate to the appearance of MAULs (i.e., can a MAUL be trusted or is it most often an artifact of the model)?
  - If the model precipitation forecast is poor (even in a convection-permitting numerical model), can the human forecaster apply frontogenesis and instability forecasts (i.e., mass fields) to create a more skillful precipitation forecast?

Future studies should rely on a combination of observational tools and high-resolution convection-permitting numerical simulations.

Finally, it is worth noting that after MGAS11, Environment Canada created a new type of weather warning for snow squalls not associated with a large body of water (Environment Canada 2013b), particularly designed for low-visibility and low-accumulation events such as CSB1 and CSB2. However, perhaps due to some of the previously discussed model forecast issues, a warning was not issued for either CSB1 or CSB2. Therefore, it is evident that much remains to be learned regarding properly representing snow-burst dynamics and thermodynamics in numerical models, which is of course crucial to improving forecasts and warnings.

Acknowledgments. This research has been supported by grants from the Natural Sciences and Engineering Research Council of Canada (Discovery Grant and Atmospheric Research Grant). Thanks to NCEP and NCDC for providing access to the NARR and NAM, and to Environment Canada for access to their online historical radar and climate information databases. The authors would also like to express our gratitude to Dr. Kelly Mahoney of NOAA/ESRL for her technical expertise and time during the revisions process. Finally, many thanks to Dr. Russ Schumacher of Colorado State University and two anonymous reviewers for their extremely helpful comments on revising this manuscript.

REFERENCES

Andretta, T. A., and B. Geerts, 2010: Heavy snowfall produced by topographically induced winds in the Snake River Plain of eastern Idaho: Part I: Observational analysis. *Electron. J. Severe Storms Meteor.,* **5** (3). [Available online at http://www.ejssm.org/ojs/index.php/ejssm/article/view/56/56.]

Bluestein, H., 1992: *Principles of Kinematics and Dynamics.* Vol. I, *Synoptic–Dynamic Meteorology in Midlatitudes,* Oxford University Press, 594 pp.

——, 1993: *Observations and Theory of Weather Systems.* Vol. II, *Synoptic–Dynamic Meteorology in Midlatitudes,* Oxford University Press, 431 pp.

Bryan, G. H., and J. M. Fritsch, 2000: Moist absolute instability: The sixth static stability state. *Bull. Amer. Meteor. Soc.,* **81,** 1207–1230, doi:10.1175/1520-0477(2000)081<1287:MAITSS>2.3.CO;2.

Davis, C. A., 1997: Mesoscale anticyclonic circulations in the lee of the central Rocky Mountains. *Mon. Wea. Rev.,* **125,** 2838–2855, doi:10.1175/1520-0493(1997)125<2838:MACITL>2.0.CO;2.

DeVoir, G. A., 2004: High impact sub-advisory snow events: The need to effectively communicate the threat of short duration high intensity snowfall. Preprints, *20th Conf. on Weather Analysis and Forecasting,* Seattle, WA, Amer. Meteor. Soc., P10.2. [Available online at https://ams.confex.com/ams/pdfpapers/68261.pdf.]

Doswell, C. A., III, H. E. Brooks, and R. A. Maddox, 1996: Flash flood forecasting: An ingredients-based methodology. *Wea. Forecasting,* **11,** 560–581, doi:10.1175/1520-0434(1996)011<0560:FFFAIB>2.0.CO;2.

Dudhia, J., 1989: Numerical study of convection observed during the Winter Monsoon Experiment using a mesoscale two-dimensional model. *J. Atmos. Sci.,* **46,** 3077–3107, doi:10.1175/1520-0469(1989)046<3077:NSOCOD>2.0.CO;2.

Emanuel, K. A., 1983: On assessing local conditional symmetric instability from atmospheric soundings. *Mon. Wea. Rev.,* **111,** 2016–2033, doi:10.1175/1520-0493(1983)111<2016:OALCSI>2.0.CO;2.

Environment Canada, cited 2013a: About radar. [Available online at http://www.ec.gc.ca/meteo-weather/default.asp?lang=En&n=2B931828-1.]

——, cited 2013b: Public alerting criteria. [Available online at http://www.ec.gc.ca/meteo-weather/default.asp?lang=En&n=D9553Alberta5-1.]

Ho, C., 2013: Calgary gets dump of snow as cold front moves in; 45 car crashes overnight. *Calgary Herald,* 11 January.

Hoskins, B. J., I. Draghici, and H. C. Davies, 1978: A new look at the ω-equation. *Quart. J. Roy. Meteor. Soc.,* **104,** 31–38, doi:10.1002/qj.49710443903.

Janjić, Z., 1994: The step-mountain eta coordinate model: Further developments of the convection, viscous sublayer, and turbulence closure schemes. *Mon. Wea. Rev.,* **122,** 927–945, doi:10.1175/1520-0493(1994)122<0927:TSMECM>2.0.CO;2.

——, R. Gall, and M. E. Pyle, 2010: Scientific documentation for the NMM solver. NCAR Tech. Note NCAR/TN-477+STR, 54 pp. [Available online at http://nldr.library.ucar.edu/repository/assets/technotes/TECH-NOTE-000-000-000-845.pdf.]

Kain, J. S., 2004: The Kain–Fritsch convective parameterization: An update. *J. Appl. Meteor.,* **43,** 170–181, doi:10.1175/1520-0450(2004)043<0170:TKCPAU>2.0.CO;2.

Keyser, D., M. J. Reeder, and R. J. Reed, 1988: A generalization of Petterssen's frontogenesis function and its relation to the forcing of vertical motion. *Mon. Wea. Rev.,* **116,** 762–780, doi:10.1175/1520-0493(1988)116<0762:AGOPFF>2.0.CO;2.

Kirschbaum, D. J., and D. R. Durran, 2005a: Atmospheric factors governing banded orographic convection. *J. Atmos. Sci.,* **62,** 3758–3774, doi:10.1175/JAS3568.1.

——, and ——, 2005b: Observation and modeling of banded orographic convection. *J. Atmos. Sci.,* **62,** 1463–1479, doi:10.1175/JAS3417.1.

Knievel, J. C., G. H. Bryan, and J. P. Hacker, 2007: Explicit numerical diffusion in the WRF model. *Mon. Wea. Rev.,* **135,** 3808–3824, doi:10.1175/2007MWR2100.1.

Koch, S., M. DesJardins, and P. Kocin, 1983: An interactive Barnes objective map analysis scheme for use with satellite and conventional data. *J. Climate Appl. Meteor.,* **22,** 1487–1503, doi:10.1175/1520-0450(1983)022<1487:AIBOMA>2.0.CO;2.

Makela, A., E. Saltikoff, J. Julkunen, I. Juga, E. Gregow, and S. Niemela, 2013: Cold season thunderstorms in Finland and their effect on aviation safety. *Bull. Amer. Meteor. Soc.,* **94,** 847–858, doi:10.1175/BAMS-D-12-00039.1.

Mesinger, F., and Coauthors, 2006: North American Regional Reanalysis. *Bull. Amer. Meteor. Soc.,* **87,** 343–360, doi:10.1175/BAMS-87-3-343.

Miller, J. E., 1948: On the concept of frontogenesis. *J. Meteor.,* **5,** 169–171, doi:10.1175/1520-0469(1948)005<0169:OTCOF>2.0.CO;2.

Milrad, S. M., J. R. Gyakum, E. H. Atallah, and J. F. Smith, 2011: A diagnostic examination of the eastern Ontario and western Quebec wintertime convection of 28 January 2010. *Wea. Forecasting,* **26,** 301–318, doi:10.1175/2010WAF2222432.1.

——, E. H. Atallah, and J. R. Gyakum, 2013: Precipitation modulation by the Saint Lawrence River valley in association with transitioning tropical cyclones. *Wea. Forecasting,* **28,** 331–352, doi:10.1175/WAF-D-12-00071.1.

Moore, J. T., and G. E. Vanknowe, 1992: The effect of jet streak curvature on kinematic fields. *Mon. Wea. Rev.,* **120,** 2429–2441, doi:10.1175/1520-0493(1992)120<2429:TEOJSC>2.0.CO;2.

——, and T. E. Lambert, 1993: The use of equivalent potential vorticity to diagnose regions of conditional symmetric instability. *Wea. Forecasting,* **8,** 301–308, doi:10.1175/1520-0434(1993)008<0301:TUOEPV>2.0.CO;2.

Nicosia, D. J., and R. H. Grumm, 1999: Mesoscale band formation in three major northeastern United States snowstorms. *Wea. Forecasting,* **14,** 346–368, doi:10.1175/1520-0434(1999)014<0346:MBFITM>2.0.CO;2.

Novak, D. R., L. F. Bosart, D. Keyser, and J. S. Waldstreicher, 2004: An observational study of cold season–banded precipitation in Northeast U.S. cyclones. *Wea. Forecasting,* **19,** 993–1010, doi:10.1175/815.1.

——, J. S. Waldstreicher, D. Keyser, and L. F. Bosart, 2006: A forecast strategy for anticipating cold season mesoscale band formation within eastern U.S. cyclones. *Wea. Forecasting,* **21,** 3–23, doi:10.1175/WAF907.1.

——, B. A. Colle, and S. E. Yuter, 2008: High-resolution observations and model simulations of the life cyclone of an intense mesoscale snowband over the northeastern United States. *Mon. Wea. Rev.,* **136,** 1433–1456, doi:10.1175/2007MWR2233.1.

——, ——, and R. McTaggart-Cowan, 2009: The role of moist processes in the formation and evolution of mesoscale snowbands within the comma head of Northeast U.S. cyclones. *Mon. Wea. Rev.,* **137,** 2662–2686, doi:10.1175/2009MWR2874.1.

——, ——, and A. R. Aiyyer, 2010: Evolution of mesoscale precipitation band environments within the comma head of Northeast U.S. cyclones. *Mon. Wea. Rev.,* **138,** 2354–2374, doi:10.1175/2010MWR3219.1.

Pettegrew, B. P., P. S. Market, R. A. Wolf, R. L. Holle, and N. W. S. Demetriades, 2009: A case study of severe winter convection in the Midwest. *Wea. Forecasting,* **24,** 121–139, doi:10.1175/2008WAF2007103.1.

Sanders, F., and B. J. Hoskins, 1990: An easy method for estimation of Q-vectors from weather maps. *Wea. Forecasting,* **5,** 346–353, doi:10.1175/1520-0434(1990)005<0346:AEMFEO>2.0.CO;2.

Schultz, D. M., and P. N. Schumacher, 1999: The use and misuse of conditional symmetric instability. *Mon. Wea. Rev.,* **127,** 2709–2732, doi:10.1175/1520-0493(1999)127<2709:TUAMOC>2.0.CO;2.

——, and J. A. Knox, 2007: Banded convection caused by frontogenesis in a conditionally, symmetrically, and inertially unstable environment. *Mon. Wea. Rev.,* **135,** 2095–2109, doi:10.1175/MWR3400.1.

Schumacher, R. S., D. M. Schultz, and J. A. Knox, 2010: Convective snowbands downstream of the Rocky Mountains in an environment with conditional, dry symmetric, and inertial instabilities. *Mon. Wea. Rev.,* **138,** 4416–4438, doi:10.1175/2010MWR3334.1.

Skamarock, W. C., and Coauthors, 2008: A description of the Advanced Research WRF version 3. NCAR Tech. Note NCAR/TN–475+STR, 113 pp. [Available online at http://www.mmm.ucar.edu/wrf/users/docs/arw_v3.pdf.]

Wetzel, S. W., and J. E. Martin, 2001: An operational ingredients-based methodology for forecasting midlatitude winter season precipitation. *Wea. Forecasting,* **16,** 156–167, doi:10.1175/1520-0434(2001)016<0156:AOIBMF>2.0.CO;2.

Wood, D., 2011: Snow causes traffic chaos. *Calgary Sun,* 3 December.

CORRIGENDUM

SHAWN M. MILRAD

Applied Aviation Sciences Department, Embry-Riddle Aeronautical University, Daytona Beach, Florida

JOHN R. GYAKUM

Department of Atmospheric and Oceanic Sciences, McGill University, Montreal, Quebec, Canada

KELLY LOMBARDO

Department of Marine Sciences, University of Connecticut—Avery Point, Groton, Connecticut

EYAD H. ATALLAH

Department of Atmospheric and Oceanic Sciences, McGill University, Montreal, Quebec, Canada

(Manuscript received and in final form 15 August 2015)

In Milrad et al. (2014), it should be clarified that the ''cold conveyor belt'' of extratropical cyclones was intended to refer to a region and not a process. A more precise term is ''comma head'' so as to indicate the specific location within the extratropical cyclone to which we are referring. As Schultz (2001) pointed out, it is actually the warm conveyor belt that is associated with ascent and therefore banded precipitation in the comma-head region of extratropical cyclones.

In addition, we note that the frontogenesis definition presented in Eq. (1) of Milrad et al. (2014) was originally formulated by Petterssen (1936), to which paper Keyser et al. (1988) later refer in the derivation of the **Q**-vector components. Also, with regard to ingredients-based methodologies, the comments of Schultz et al. (2002) should be considered by the reader, especially in the context of Wetzel and Martin (2001).

REFERENCES

Keyser, D., M. J. Reeder, and R. J. Reed, 1988: A generalization of Petterssen's frontogenesis function and its relation to the forcing of vertical motion. *Mon. Wea. Rev.*, **116**, 762–780, doi:10.1175/1520-0493(1988)116<0762:AGOPFF>2.0.CO;2.

Milrad, S. M., J. R. Gyakum, K. Lombardo, and E. H. Atallah, 2014: On the dynamics, thermodynamics, and forecast model evaluation of two snow burst events in southern Alberta. *Wea. Forecasting*, **29**, 725–749, doi:10.1175/WAF-D-13-00099.1.

Petterssen, S., 1936: Contribution to the theory of frontogenesis. *Geophys. Publ.*, **11** (6), 1–27.

Schultz, D. M., 2001: Reexamining the cold conveyor belt. *Mon. Wea. Rev.*, **129**, 2205–2225, doi:10.1175/1520-0493(2001)129<2205:RTCCB>2.0.CO;2.

——, J. V. Cortinas Jr., and C. A. Doswell III, 2002: Comments on ''An operational ingredients-based methodology for forecasting midlatitude winter season precipitation.'' *Wea. Forecasting*, **17**, 160–167, doi:10.1175/1520-0434(2002)017<0160:COAOIB>2.0.CO;2.

Wetzel, S. W., and J. E. Martin, 2001: An operational ingredients-based methodology for forecasting midlatitude winter season precipitation. *Wea. Forecasting*, **16**, 156–167, doi:10.1175/1520-0434(2001)016<0156:AOIBMF>2.0.CO;2.

Corresponding author address: Shawn M. Milrad, Applied Aviation Sciences Dept., Embry-Riddle Aeronautical University, 600 S. Clyde Morris Blvd., Daytona Beach, FL 32119.
E-mail: shawn.milrad@gmail.com

DOI: 10.1175/WAF-D-15-0106.1